CORONAVIRUS

Core mitochondrial genes are down-regulated during SARS-CoV-2 infection of rodent and human hosts

Joseph W. Guarnieri[1,2,3], Joseph M. Dybas[2,3], Hossein Fazelinia[2,3], Man S. Kim[1,2,3,4], Justin Frere[5], Yuanchao Zhang[1,2,3], Yentli Soto Albrecht[1,2,3], Deborah G. Murdock[1,2], Alessia Angelin[1,2], Larry N. Singh[1,2,3], Scott L. Weiss[1,2], Sonja M. Best[3,6], Marie T. Lott[1,2], Shiping Zhang[1,2], Henry Cope[7], Victoria Zaksas[3,8,9], Amanda Saravia-Butler[3,10,11], Cem Meydan[3,12], Jonathan Foox[12], Christopher Mozsary[12], Yaron Bram[12], Yared Kidane[3,13], Waldemar Priebe[3,14], Mark R. Emmett[3,15], Robert Meller[3,16], Sam Demharter[17], Valdemar Stentoft-Hansen[17], Marco Salvatore[17], Diego Galeano[3,18], Francisco J. Enguita[3,19], Peter Grabham[20], Nidia S. Trovao[3,21], Urminder Singh[3,22], Jeffrey Haltom[1,2,3,22], Mark T. Heise[23], Nathaniel J. Moorman[23], Victoria K. Baxter[23], Emily A. Madden[23], Sharon A. Taft-Benz[23], Elizabeth J. Anderson[23], Wes A. Sanders[23], Rebekah J. Dickmander[23], Stephen B. Baylin[3,24], Eve Syrkin Wurtele[3,22], Pedro M. Moraes-Vieira[3,25], Deanne Taylor[1,2,3], Christopher E. Mason[3,12,26], Jonathan C. Schisler[3,23], Robert E. Schwartz[3,12], Afshin Beheshti[3,27,28]†*, Douglas C. Wallace[1,2,3,29]†*

Severe acute respiratory syndrome coronavirus 2 (SARS-CoV-2) viral proteins bind to host mitochondrial proteins, likely inhibiting oxidative phosphorylation (OXPHOS) and stimulating glycolysis. We analyzed mitochondrial gene expression in nasopharyngeal and autopsy tissues from patients with coronavirus disease 2019 (COVID-19). In nasopharyngeal samples with declining viral titers, the virus blocked the transcription of a subset of nuclear DNA (nDNA)–encoded mitochondrial OXPHOS genes, induced the expression of microRNA 2392, activated HIF-1α to induce glycolysis, and activated host immune defenses including the integrated stress response. In autopsy tissues from patients with COVID-19, SARS-CoV-2 was no longer present, and mitochondrial gene transcription had recovered in the lungs. However, nDNA mitochondrial gene expression remained suppressed in autopsy tissue from the heart and, to a lesser extent, kidney, and liver, whereas mitochondrial DNA transcription was induced and host-immune defense pathways were activated. During early SARS-CoV-2 infection of hamsters with peak lung viral load, mitochondrial gene expression in the lung was minimally perturbed but was down-regulated in the cerebellum and up-regulated in the striatum even though no SARS-CoV-2 was detected in the brain. During the mid-phase SARS-CoV-2 infection of mice, mitochondrial gene expression was starting to recover in mouse lungs. These data suggest that when the viral titer first peaks, there is a systemic host response followed by viral suppression of mitochondrial gene transcription and induction of glycolysis leading to the deployment of antiviral immune defenses. Even when the virus was cleared and lung mitochondrial function had recovered, mitochondrial function in the heart, kidney, liver, and lymph nodes remained impaired, potentially leading to severe COVID-19 pathology.

INTRODUCTION

The coronavirus disease 2019 (COVID-19) pandemic has been responsible for more than 6.9 million deaths worldwide and has infected more than 677 million people as of 25 June 2023. COVID-19 is caused by the single-stranded RNA virus, severe acute respiratory syndrome coronavirus 2 (SARS-CoV-2), whose 30-kDa genome encodes four structural proteins (S, M, E, and N), 16 nonstructural proteins (NSPs), and nine additional open reading frames (ORFs). Whereas COVID-19 is primarily considered an inflammatory disease, recent evidence suggests that SARS-CoV-2 inhibits mitochondrial function (*1*–*4*), consistent with a central role for mitochondria in cellular metabolism and innate immune regulation (*5*, *6*). SARS-CoV-2 infection markedly alters mitochondrial morphology, with matrix condensation and swollen cristae. This is associated with decreased oxidative phosphorylation (OXPHOS) polypeptides, decreased mitochondrial inner membrane protein import systems, and increased production of mitochondrial reactive oxygen species (mROS) (*7*–*9*).

The mitochondrion generates energy by OXPHOS, which encompasses about 160 polypeptides, most dispersed across the chromosomes, but with 13 critical polypeptides encoded by the maternally inherited mitochondrial DNA (mtDNA). These mtDNA polypeptides are translated on mitochondrial ribosomes using mtDNA-encoded ribosomal RNAs (rRNAs) and the tRNAs that punctuate the polypeptide genes. Nuclear DNA (nDNA) encodes more than one thousand mitochondrial genes whose proteins are synthesized on cytosolic ribosomes and imported into the mitochondrion through the translocase of the outer mitochondrial membrane (TOMM) and inner mitochondrial membrane (TIMM) import complexes.

OXPHOS encompasses four electron transport chain enzyme complexes (I, II, III, and IV) plus the adenosine 5′-triphosphate (ATP) synthase (complex V). Complexes I, III, IV, and V are assembled from both nDNA- and mtDNA-encoded proteins, and all of the multi-subunit OXPHOS complexes are assembled via intermediate-stage subassembly modules, often requiring specific assembly

factors (*10*–*12*). Complex I incorporates seven mtDNA (*MT-ND1*, *MT-ND2*, *MT-ND3*, *MT-ND4L*, *MT-ND4*, *MT-ND5*, and *MT-ND6*) subunits and is assembled in six subassembly modules. Four modules nucleate around mtDNA-coded polypeptides, MT-ND1, MT-ND2, MT-ND4, and MT-ND5, plus the Q and N modules. Complex II is assembled exclusively from four nDNA-coded subunits. Complex III encompasses one mtDNA subunit, MT-CYB, and 10 nDNA structural subunits and is assembled in stages. Complex IV incorporates three mtDNA subunits, MT-CO1, MT-CO2, and MT-CO3, each of which nucleates one of the three subassembly modules, using multiple assembly factors including *SCO2*. Complex V encompasses two mtDNA polypeptides, MT-ATP6 and MT-ATP8, and is assembled from five subassembly modules.

SARS-CoV-2 viral polypeptides bind to multiple host polypeptides, up to 16% of which are mitochondrial proteins (*13*–*15*). For example, the SARS-CoV-2 M protein interacts with the mitochondrial leucyl-tRNA (*TARS2*) and asparaginyl-tRNA (*NARS2*) synthases and the coenzyme Q (CoQ) synthesis protein *COQ8B*. The SARS-CoV-2 N protein binds to the import peptidases PMPCA plus PMPCB and several complex I subunits. The SARS-CoV-2 nonstructural protein, NSP6, binds to complex V subunits. SARS-CoV-2 open reading frame ORF10 binds to TIMM8, and ORF9b binds to TOMM70 (*13*–*17*).

SARS-CoV-2–infected mice expressing the human angiotensin-converting enzyme 2 receptor (K18-hACE2 mice) have reduced nDNA- and mtDNA-encoded mitochondrial OXPHOS proteins in the heart, lung, kidney, and spleen (*18*). SARS-CoV-2–infected human cells and tissues exhibit decreased proteins and transcripts of OXPHOS genes in association with increased expression of glycolytic proteins (*7*, *19*, *20*). In human blood cells, SARS-CoV-2 infection is associated with down-regulation of mtDNA transcripts, mitochondrial function, and increased glycolysis (*21*), together with suppression of OXPHOS, increased mROS production, increased mRNAs of inflammation factors, and increased hypoxia inducing factor–1α (HIF-1α) and HIF-1α target genes (*22*). In other human cells and tissues, SARS-CoV-2 infection also increased the transcription of both HIF-1α and HIF-1α glycolytic target genes (*15*, *20*, *23*, *24*); HIF-1α inhibitors, chetomin or BAY 87-2243, reduced HIF-1α induction of glycolytic gene expression and inhibited viral replication (*22*, *24*, *25*). SARS-CoV-2 inhibition of OXPHOS results in increased mROS, which activates HIF-1α, leading to impaired OXPHOS and increased glycolysis (*26*).

Shifting cell substrates from glucose to galactose or treatment with the glycolysis inhibitor 2-deoxy-D-glucose reduced SARS-CoV-2 replication (*19*, *23*, *27*). In contrast, treatment with the OXPHOS complex V inhibitor, oligomycin, increased viral load and cytokine and interferon production. Moreover, treatment with the ROS scavengers *N*-acetyl cysteine (NAC) and MitoQ reduced HIF-1α, glycolytic proteins, pro-inflammatory cytokine mRNAs, and viral load (*22*). The mammalian target of rapamycin complex 1 (mTORC1) stimulated nutrient uptake favoring glycolytic metabolism by activating c-Myc, stabilizing HIF-1α, and impairing mitochondrial biogenesis (*28*, *29*). SARS-CoV-2–infected lung tissue and cell lines have increased mTORC1, and treatment with an mTORC1 inhibitor, rapamycin, decreased viral replication (*30*).

Impairment of mitochondrial protein synthesis can result in an imbalance in the ratio of nDNA- and mtDNA-coded mitochondrial proteins, which can activate the mitochondrial (UPR^{MT}) and the cytosolic (UPR^{CT}) unfolded protein responses (*31*), which will, in turn, trigger the integrated stress response (ISR). The ISR can be activated by single-strand viral RNA binding to the RNA-activated protein kinase (PKR) or by UPR^{MT} activation of the mitochondrial protease OMA1 to cleave DELE1, activating the ISR heme regulated initiation factor 2 alpha (HRI) kinase (*32*–*34*). When activated, these kinases phosphorylate the mitochondrial initiation factor eIF2α, which impairs general cytosolic protein synthesis while facilitating the translation of activating transcription factors 4/5 (ATF4/5) (*35*, *36*). Activation of ATP4/5 induces *GADD34*, *CHOP*, and the mitokines fibroblast growth factor 21 (FGF21) and growth and differentiation factor 15 (GDF15) (*37*, *38*), as well as inducing OXPHOS supercomplex assembly factor SCAF1 (*39*). SARS-CoV-2 infection activates the ISR and is associated with elevated FGF21 (*40*) and GDF15 (*41*).

Although there is considerable evidence indicating that SARS-CoV-2 polypeptides bind to mitochondrial proteins, there is limited information on the effects of the virus on mitochondrial gene transcription, which has resulted in apparent inconsistencies (*20*). We, therefore, investigated the effects of SARS-CoV-2 infection on transcription of host genes for mitochondrial OXPHOS, glycolysis, nutrient sensing, and the stress response in nasopharyngeal specimens from individuals with early SARS-CoV-2 infection and in autopsy tissue samples from individuals with late-stage infection, collected during the pandemic in New York City (*42*). We also used SARS-CoV-2–infected hamsters and SARS-CoV-2–infected BALB/c and C57BL/6 mice to analyze changes in host bioenergetic gene expression at the early and mid-stages of virus infection.

[1]Center for Mitochondrial and Epigenomic Medicine, Children's Hospital of Philadelphia, Philadelphia, PA 19104, USA. [2]Children's Hospital of Philadelphia, Philadelphia, PA 19104, USA. [3]COVID-19 International Research Team, Medford, MA 02155, USA . [4]Kyung Hee University Hospital at Gangdong, Kyung Hee University, Seoul, South Korea. [5]Icahn School of Medicine at Mount Sinai, New York, NY 10023, USA. [6]Rocky Mountain Laboratory, National Institute of Allergy and Infectious Disease, NIH, Hamilton, MT 59840, USA. [7]University of Nottingham, Nottingham, UK. [8]University of Chicago, Chicago, IL 60615, USA. [9]Clever Research Lab, Springfield, IL 62704, USA. [10]Logyx, LLC, Mountain View, CA 94043, USA. [11]NASA Ames Research Center, Moffett Field, CA 94035, USA. [12]Weill Cornell Medicine, New York, NY 10065, USA. [13]Texas Scottish Rite Hospital for Children, Dallas, TX 75219, USA. [14]University of Texas MD Anderson Cancer Center, Houston, TX 77030, USA. [15]University of Texas Medical Branch, Galveston, TX 77555, USA. [16]Morehouse School of Medicine, Atlanta, GA 30310, USA. [17]DKAbzu ApS, Copenhagen 2150, Denmark. [18]Facultad de Ingeniería, Universidad Nacional de Asunción, San Lorenzo, Central, Paraguay. [19]Faculdade de Medicina, Universidade de Lisboa, Instituto de Medicina Molecular João Lobo Antunes, 1649-028 Lisboa, Portugal. [20]College of Physicians and Surgeons, Columbia University, New York, NY 19103, USA. [21]Fogarty International Center, National Institutes of Health, Bethesda, MD 20892, USA. [22]Iowa State University, Ames, IA 50011, USA. [23]University of North Carolina at Chapel Hill, Chapel Hill, NC 27599, USA. [24]Johns Hopkins School of Medicine, Baltimore, MD 21287, USA. [25]University of Campinas, Campinas, SP, Brazil. [26]New York Genome Center, New York, NY 10013, USA. [27]Stanley Center for Psychiatric Research, Broad Institute of MIT and Harvard, Cambridge, MA 02142, USA. [28]KBR, Space Biosciences Division, NASA Ames Research Center, Moffett Field, CA 94035, USA. [29]Division of Human Genetics, Department of Pediatrics, University of Pennsylvania, Philadelphia, PA 19104, USA.
*Corresponding author. Email: wallaced1@chop.edu (D.C.W.); afshin.beheshti@cov-int.org (A.B.)
†These authors contributed equally to this work.

RESULTS

Changes in OXPHOS gene transcription in COVID-19 human nasopharyngeal samples

First, we determined the effects of SARS-CoV-2 early-stage infection in human hosts. We compared the gene expression profiles of about 700 nasopharyngeal samples, including SARS-CoV-2–infected cases versus uninfected control cases collected in New York City from 2018 to 2020. The COVID-19 cases were subdivided into high, medium, and low SARS-CoV-2 viral loads (fig. S1). Analysis of transcription in the infected nasopharyngeal samples revealed that SARS-CoV-2 inhibited the gene expression of all five OXPHOS complexes (complexes I to V). This was evident for the high and medium viral load samples but not for the lowest viral load samples (Fig. 1A).

To determine the mechanism by which SARS-CoV-2 inhibited each of the OXPHOS complexes, we examined the mRNAs of individual mitochondrial and bioenergetic polypeptide genes (table S1). This revealed that SARS-CoV-2 infection suppressed the expression of groups of human genes associated with specific OXPHOS subassembly modules. This contrasted with the up-regulation of host mitochondrial genes not inhibited by the virus that frequently included either structural or assembly genes of subassembly modules not blocked by infection (Fig. 1, B and C). This suggested that groups of subassembly module structural and assembly gene mRNAs may be coordinately regulated and that these coordinately regulated genes could be modulated by SARS-CoV-2 (Fig. 1C), with the degree of SARS-CoV-2 perturbation proportional to viral load (Fig. 1B).

For complex I, the nDNA subunit genes were incorporated into six subassembly modules, four of which were nucleated around mtDNA coded polypeptides (MT-ND1, MT-ND2, MT-ND4, and MT-ND5) (table S1). SARS-CoV-2 down-regulated four of the five structural genes of the MT-ND2 module, whereas five of the six assembly factors were up-regulated. All six structural subunit genes of the MT-ND4 module were down-regulated, but assembly factor gene *DMAC2* was up-regulated. All of the MT-ND5 module's nDNA-coded genes were down-regulated, as were 7 of the 11 N module nDNA genes. By contrast, two of the six nDNA genes of the MT-ND1 module were strongly up-regulated, whereas half of the nDNA genes of the Q module were up-regulated and half were down-regulated (Fig. 1B). These coordinate changes in structural and assembly genes were found to be significant by QLattice analysis with $P < 0.05$ (Fig. 1C).

For complex II, the structural subunit genes *SDHC* and *SDHD* were strongly down-regulated, whereas *SDHA* and *SDHB* subunits were not. Assembly factors *SDHAF3* and *SDHAF4* were down-regulated, whereas assembly factors *SDHAF1* and *SDHAF2* were not (Fig. 1, B and C, and table S1). For complex III, all nDNA structural genes were down-regulated except the *CYC1* gene, which was up-regulated. The central assembly factors *UQCC1*, *UQCC2*, and *UQCC3* were up-regulated, whereas assembly factors *LYRM7*, *BCS1L*, and *TTC19* were down-regulated (Fig. 1, B and C, and

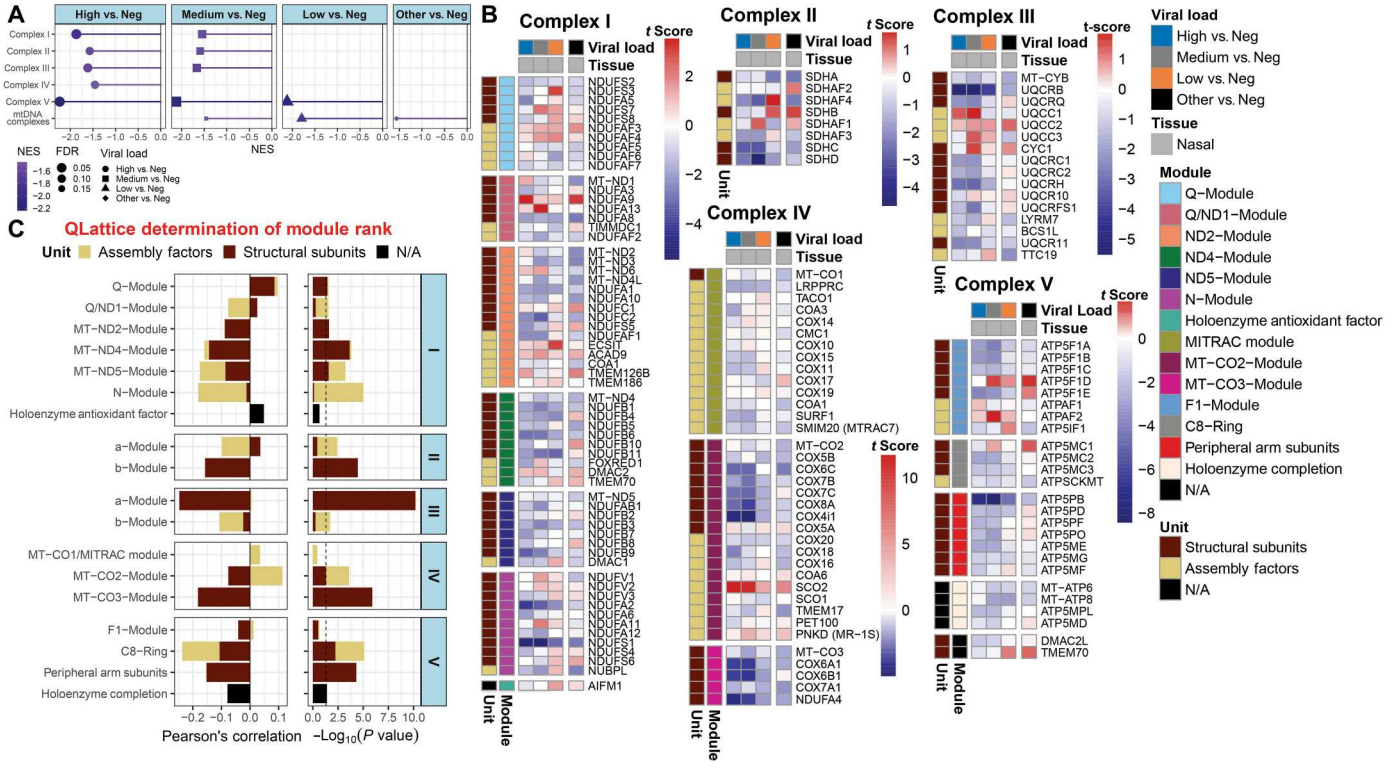

Fig. 1. Mitochondrial OXPHOS complex gene expression in nasopharyngeal samples from patients with COVID-19. (**A**) Lollipop plots of custom-curated mitochondria gene sets were determined by fGSEA for nasopharyngeal samples from patients with COVID-19 and were ranked by nominal enrichment score (NES). The size of the symbols represents the FDR. (**B**) Heatmaps of *t*-score statistics for specific mitochondrial complex gene expression are shown. (**C**) Coordinate changes in clusters of OXPHOS structural and assembly genes by QLattice analysis show the directional changes of the specific OXPHOS modules by Pearson's correlation and the statistical significance by $-\log_{10}$ (*P* value).

table S1). For complex IV, all four nDNA genes of the MT-CO3 module were down-regulated. A cluster of six genes of the MT-CO2 module was strongly down-regulated, whereas assembly factor *SCO2* was strongly up-regulated. Genes of the MT-CO1 module were minimally affected (Fig. 1, B and C, and table S1). For complex V, nearly all of the nDNA genes in modules ATP5MC1, ATP5PB, and MT-ATP6/8, as well as the assembly factors *DMAC2L* and *TMEM70*, were down-regulated, with the *ATP5PB* gene being strongly suppressed. Last, four of the five structural genes of the ATP5F1A module were down-regulated, whereas two of the three assembly factors were up-regulated (Fig. 1, B and C, and table S1).

We further analyzed human nasopharyngeal samples for the effects of SARS-CoV-2 infection on mRNAs for all known mitochondrial genes (table S2) (*43*, *44*). The resulting volcano plots demonstrated the effects of decreasing viral copy number on host mitochondrial gene expression (fig. S2). At high viral load, the most notable changes in mitochondrial gene expression were the strong suppression of *ALAS2*, one of the 5′-aminolevulinate synthetases involved in heme synthesis; strong induction of the complex IV assembly factor, *SCO2*; and up-regulation of the mitochondrial genes thought to be important in the mitochondrial induction of the innate immune response (fig. S2A). These virally induced mitochondrial innate immune regulatory genes included *PNPT1* (polyribonucleotide nucleotidyltransferase 1), which may release mitochondrial double-stranded RNA to engage melanoma differentiation-associated protein 5 (IFIH1) and trigger the type I interferon response (fig. S2) (*45*); *CMPK2* (cytosine monophosphate kinase 2), which is the rate-limiting step for the induction of mtDNA replication creating oxidized mtDNA (Ox-mtDNA), which is released from mitochondria and binds to the inflammasome (*6*); *ACOD1* (aconitate decarboxylase 1 or *IRG1*), which regulates itaconate production and modulates inflammatory myeloid cells (*46*); and *IFI27* (interferon alpha inducible protein 27), which activates interferon expression and is a diagnostic blood marker for SARS-CoV-2 infection (fig. S2) (*47*). Hence, SARS-CoV-2 not only inhibited OXPHOS but also activated mitochondrial innate immunity signaling genes (*CMPK2*, *PNPT1*, *IFI27*, and *IRG1*) (fig. S2B). The acute transcriptional changes observed in SARS-CoV-2 human nasopharyngeal infection were also reflected in the transcripts/proteins of acutely infected CaCo-2 cells (fig. S3, A and B) (*47*) and blood samples from patients with COVID-19 (fig. S3, C and D).

Changes in OXPHOS gene transcription in COVID-19 human autopsy samples

We next analyzed mitochondrial bioenergetic gene expression in autopsy samples of the hearts, kidneys, livers, lungs, and lymph nodes from 35 deceased individuals who had COVID-19 compared with five uninfected control individuals. The patients with COVID-19 had either high or low SARS-CoV-2 infection rates upon hospital admission (fig. S1). Monocyte data from patients with COVID-19 were also included in the analysis (Fig. 2) (*48*).

OXPHOS mRNAs were down-regulated in the COVID-19 autopsy samples of the heart, liver, kidney, and lymph nodes, with the heart exhibiting the most coordinated down-regulation of OXPHOS gene expression. In contrast, the autopsy lung samples showed an equally large up-regulation of OXPHOS gene expression (Fig. 2A). Analysis of individual OXPHOS complex subassembly module structural and assembly genes (Fig. 2B and table S1) confirmed that virtually all OXPHOS mRNAs of the heart were shut down (Fig. 2B). This was not simply the product of terminal destruction of heart cells because mtDNA transcripts and the COX assembly gene mRNAs, *COX16*, *COX19*, and *COX20*, were up-regulated and *PET100* and *SCO2* were normally expressed (Fig. 2B). The OXPHOS mRNA profiles in the COVID-19 autopsy samples of the kidney and liver (Fig. 2, B and C) were similar. Both showed down-regulation of selected complex I structural genes in the MT-ND1, MT-ND2, MT-ND4, MT-ND5, N, and Q modules, complex II *SDHA*, and complex III structural and assembly genes *CYC1*, *UQCRC1*, *BCS1L*, and *TTC19* (Fig. 2, B and C). This shared transcriptional profile suggests the possibility that transcriptional regulatory elements coordinately regulate groups of OXPHOS genes. The lymph nodes also showed down-regulation of subsets of modular mRNAs (Fig. 2, B and C) including those in complex I modules NDUFS2, MT-ND1, and MT-ND2; *SDHC* and *SDHD* in complex II; and *CMC1* and *COX20* in complex IV modules MT-CO1 and MTCO2 (Fig. 2B). OXPHOS gene expression was strongly up-regulated in COVID-19 autopsy lung samples (Fig. 2, B and C) (*20*) in apposition to nasopharyngeal samples and other autopsy tissues. Complex I, II, and III genes were particularly robustly up-regulated in COVID-19 autopsy lung samples (Fig. 2, B and C), including *SDHB*, *SDHD*, *SDHAF3*, and *SDHAF4* of complex II, and most of the structural genes of complex III as well as the *UQCC2* and *UQCC3* assembly genes (Fig. 2, B and C). The structural genes of the complex IV MT-CO2 and MT-CO3 modules and the *SCO2* assembly gene were up-regulated, as were the structural genes of the ATP5PB, MT-ATP6/8, and ATP5MC1 and the structural and assembly genes of the ATP5F1A modules of complex V (Fig. 2, B and C).

Thus, nDNA-coded OXPHOS gene transcripts were down-regulated in autopsy tissues with heart > > kidney = liver > lymph node, but, in autopsy lung samples, OXPHOS genes were strongly induced (Fig. 2, A to C). In the nasopharyngeal samples, the high-titer virus samples experienced strong OXPHOS gene inhibition (Fig. 1, B and C, and fig. S2A), but this inhibition was lifted in the lung autopsy tissue as the virus was cleared (Fig. 2, B and C, and fig. S1B). In contrast, in the human autopsy heart, kidney, liver, and lymph nodes, OXPHOS gene suppression continued even though the virus had been eliminated (Fig. 2, B and C, and fig. S1B).

The coordinated regulation of the structural and assembly genes of the OXPHOS modules was supported by their opposite directional transcriptional expression in several OXPHOS complex submodules (Fig. 2C). This was seen for the complex I modules: Q module in human lymph nodes; MT-ND1 module in the human kidney, liver, and lung; MT-ND2 module in the human lymph nodes; MT-ND5 module in the human kidney; and N module in the human lymph nodes. Similar opposing structural and assembly gene bidirectional transcriptional changes were seen for complexes II, III, and IV, with the differences significant by QLattice analysis (with $P < 0.05$, indicated by the vertical dashed lines in Fig. 2C). The SARS-CoV-2–induced changes in OXPHOS genes in autopsy tissues from patients with COVID-19 were sufficiently robust that specific pairs of genes proved sufficient to discriminate between infected and uninfected tissues (fig. S4, A and B). For example, *SLC25A16* versus *LDHB* could differentiate infected from uninfected heart tissue, and *MUCB* versus *ALAS2* could differentiate infected from uninfected kidney tissue (fig. S4B).

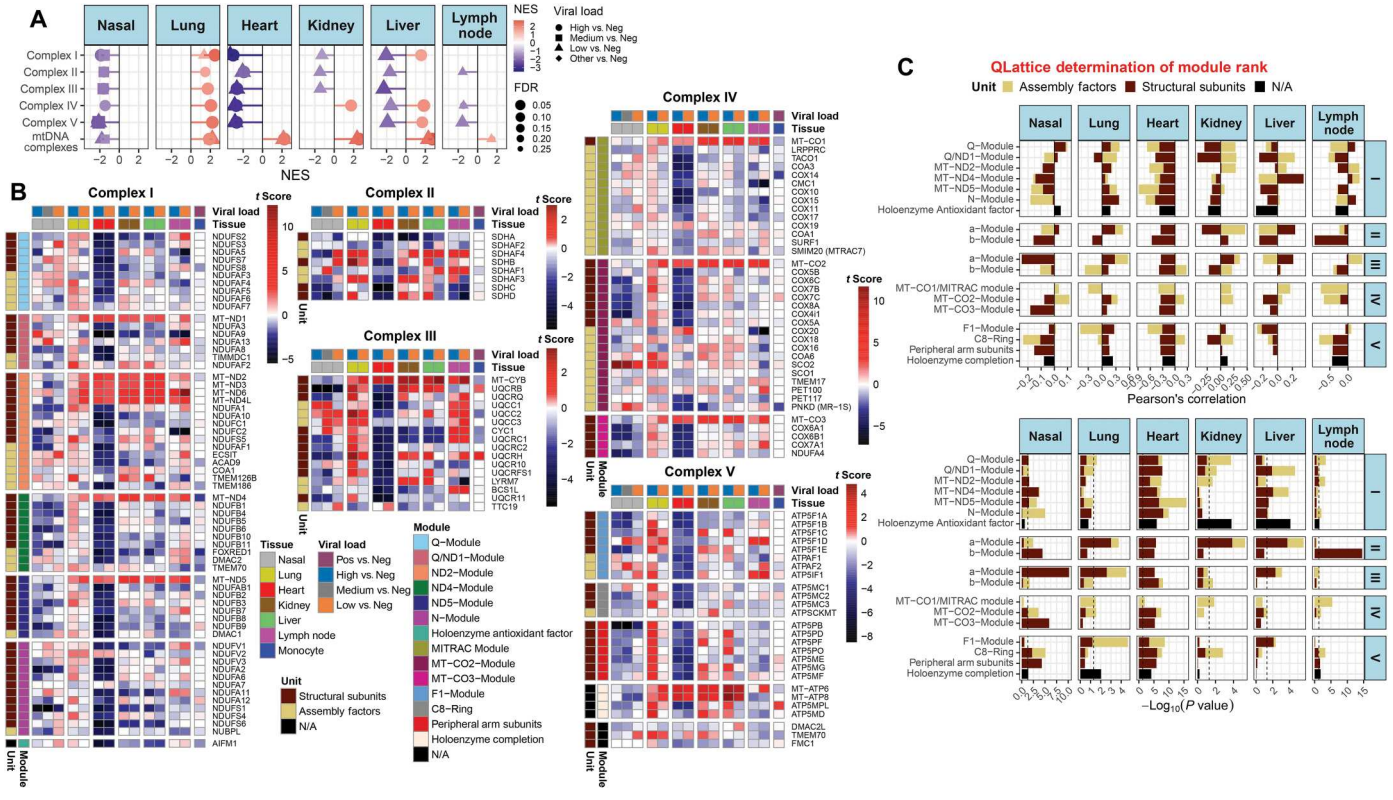

Fig. 2. Mitochondrial OXPHOS complex gene expression in nasopharyngeal samples and autopsy tissues from patients with COVID-19. (**A**) Lollipop plots for statistically significant changes in custom mitochondria and MitoPathway gene sets were determined by fGSEA for nasopharyngeal samples and autopsy tissues from patients with COVID-19 and were ranked by NES. The size of the symbols represents the FDR. (**B**) Heatmaps display the *t*-score statistics for specific mitochondrial OXPHOS complex genes when comparing autopsy tissue and nasopharyngeal samples from COVID-19–positive and COVID-19–negative patients. (**C**) Coordinate changes in clusters of OXPHOS structural and assembly genes by QLattice analysis show the directional changes in gene expression by Pearson's correlation and the statistical significance by $-\log_{10}$ (*P* value).

We next analyzed the changes in mRNAs in COVID-19 human autopsy samples for all known mitochondrial genes (*43*, *44*) using volcano plots (fig. S5, A and B). Mitochondrial gene expression was reduced in autopsy tissues from patients admitted to the hospital with high compared with low viral loads, which confirmed that the extent of altered mitochondrial gene expression may be regulated by viral load (fig. S5). Down-regulation of mitochondrial pathways in response to virus in human autopsy samples was most extensive in hearts followed in decreasing order by the kidneys, livers, and lymph nodes (fig. S5). This inhibition of mitochondrial gene expression in visceral autopsy tissues parallels that seen in the nasopharyngeal samples with high viral titer but in the absence of a detectable virus. The lung exhibited increased mitochondrial gene expression profiles consistent with the release of inhibition of mitochondrial gene expression upon clearance of the virus (fig. S6).

In relation to viral activation of mitochondrial innate immunity, the *C15orf48* mRNA was up-regulated in the human heart autopsy tissue from patients with COVID-19. C15orf48 is a complex IV protein that upon viral infection displaces NDUFA4 and induces expression of microRNA 147b (miR-147b), which inhibits *NDUFA4* translation and enhances RIG-1/MDA-5–mediated antiviral immunity (*49*). This antiviral response parallels the induction of antiviral genes in the human COVID-19 nasopharyngeal samples. The mitochondrial calcium uniporter *MCUB* and vitamin D metabolism were up-regulated in the heart, folate metabolism was up-regulated in the lung, and the heme synthesis *ALAS2* gene was strongly up-regulated in the heart, kidney, liver, and lung autopsy samples (fig. S5).

SARS-CoV-2 modulation of mitochondrial and glycolytic pathways in human nasopharyngeal and autopsy samples

We next focused on transcriptional changes in processes that complement mitochondrial OXPHOS, including mitochondrial ATP/ADP-Pi exchange, tricarboxylic acid (TCA) cycle, CoQ biosynthesis, mitochondrial fatty acid synthesis (mtFASII), fatty acid oxidation, and the cytosolic protein import system (Fig. 3A). Overall, autopsy heart tissue from patients with SARS-CoV-2 infection showed a systematic down-regulation of genes involved in multiple mitochondrial functions; this was also found, to a lesser extent, in kidneys and livers and, to the least extent, in nasopharyngeal samples and lymph node autopsy samples. The lung autopsy samples showed down-regulation of CoQ synthesis and mtFASII but up-regulation of genes involved in the TCA cycle and cytosolic protein import (Fig. 3A).

At the individual gene level (Fig. 3B and fig. S6), key mitochondrial inner membrane solute carrier genes were down-regulated in the heart, including the phosphate carrier (*SLC25A3*), the adenine nucleotide translocases (*SLC25A4* and *SLC25A6*), the citrate carrier

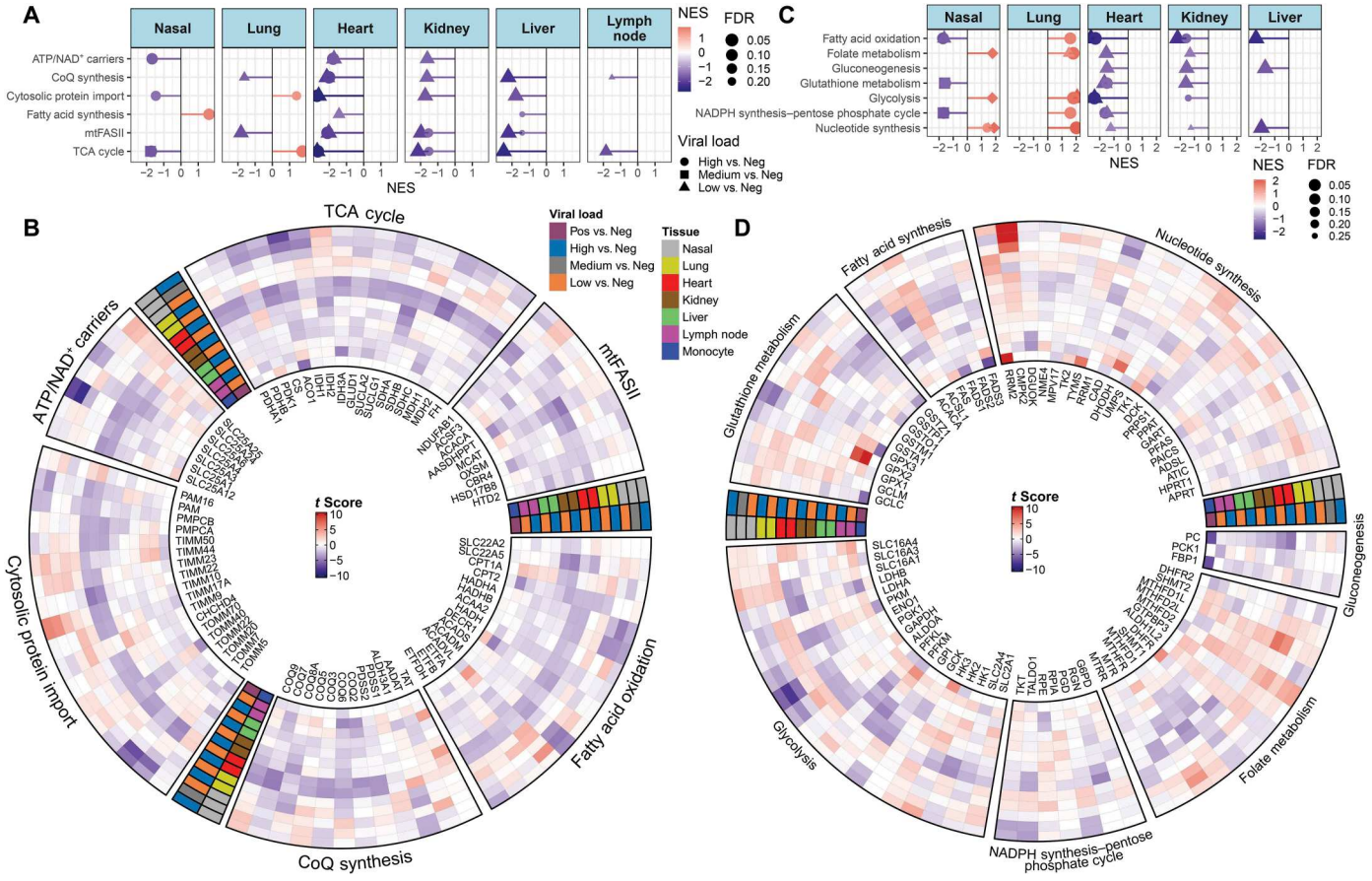

Fig. 3. Mitochondrial and cytosolic bioenergetic pathway gene expression in nasopharyngeal and autopsy samples from patients with COVID-19. (**A**) Lollipop plots for statistically significant custom mitochondria and MitoPathway bioenergetic gene sets were determined by fGSEA for nasopharyngeal samples and autopsy tissues (lung, heart, kidney, liver, and lymph node) from patients with COVID-19 and were ranked by NES. (**B**) The circular heatmap displays the *t*-score statistics for mitochondrial metabolic pathway genes when comparing nasopharyngeal and autopsy samples from patients with and without COVID-19. (**C**) Lollipop plots for statistically significant changes in cellular metabolic gene sets were determined by fGSEA for nasopharyngeal and autopsy tissues from patients with COVID-19 and were ranked by NES. (**D**) The circular heatmap displays the *t*-score statistics for cytosolic metabolic genes when comparing nasopharyngeal and autopsy samples from patients with and without COVID-19.

(*SLC25A1*), and the Ca^{++}-binding aspartate-glutamate carrier (*SLC25A12*), which are critical for mitochondrial energy production and ATP export. In contrast, the ATP-Mg^{++}/Pi transporters (*SLC25A24* and *SLC25A25*), which import ATP into the mitochondria without energetic benefit, were up-regulated in human heart autopsy samples from patients with COVID-19. Similarly, human nasopharyngeal samples from patients with COVID-19 manifested the down-regulation of the phosphate carrier (*SLC25A3*) as well as ANT3 (*SLC25A6*) and the up-regulation of the ATP-Mg^{++}/Pi transporter (*SLC25A25*). Thus, as the virus inhibited mitochondrial energetics, host cells attempted to compensate by importing ATP. In contrast to the heart, kidney, and liver, ATP generation–associated genes were not perturbed in the autopsy lung samples where OXPHOS gene expression was restored (Fig. 3B and fig. S6). Similarly, the mRNAs of CoQ synthesis, the TCA cycle, fatty acid oxidation, mtFASII, and cytosolic protein import were consistently down-regulated in the heart and, to a lesser extent, in the kidneys, livers, lymph nodes, and nasopharyngeal samples, but not in the lung (Fig. 3B and fig. S6).

Expression analysis of genes associated with cytosolic bioenergetic pathways (Fig. 3, C and D) revealed that glycolysis and fatty acid synthesis transcripts were significantly down-regulated [with a false discovery rate (FDR) < 0.25] in hearts and kidneys, and fatty acid synthesis was down-regulated in livers. Folate metabolism, gluconeogenesis, and glutathione metabolism transcripts were also down-regulated in hearts and kidneys and partially in the livers (Fig. 3D). In the nasopharyngeal samples, glutathione metabolism was down-regulated, whereas, in the human autopsy lung samples, glycolysis and folate metabolism were up-regulated (Fig. 3, C and D).

Changes in mRNAs of glycolysis and pentose phosphate pathway genes were reduced in the human heart and nasopharyngeal tissues but were minimally altered in the other tissues (Fig. 3D). Among cardiac glycolytic genes in the human heart autopsy tissue, there was a normal expression of lactate dehydrogenase A (*LDHA*), which converts pyruvate to lactate and favors glycolysis, but a down-regulation of lactate dehydrogenase B (*LDHB*), which converts lactate to pyruvate and favors OXPHOS, a pattern also reported in peripheral blood (*21*). The glucose carriers *SLC2A1* and

SLC2A4 were down-regulated in the heart, as was the monocarboxylate carrier 1 (*SLC16A1*), which transports lactate across the mitochondrial inner membrane. However, monocarboxylate carrier 5 (*SLC16A4*) was up-regulated in the human heart in response to HIF-1α activation after the SARS-CoV-2 infection (Fig. 3D) (*50*). In the human nasopharyngeal samples, down-regulation of downstream glycolysis genes, *GAPDH* and *PGK1* (Fig. 3D), may have favored the retention of substrates in the earlier steps of glycolysis, which would fuel fatty acid and NADPH (reduced form of nicotinamide adenine dinucleotide phosphate) synthesis and promote viral biogenesis. Expression of single-carbon metabolism genes, which metabolically interconnect the mitochondrion with the nucleus-cytosol, revealed that, with the exception of dihydrofolate reductase 2, the mitochondrial folate enzyme genes were up-regulated in hearts, kidneys, livers, and lymph nodes. In contrast, the cytosolic and nuclear folate enzyme genes were down-regulated in hearts and less so in kidneys and livers, with lung tissue being more variable (Fig. 3D).

SARS-CoV-2 modulation of HIF-1α, mTOR, and ISR pathways in human nasopharyngeal and autopsy samples

In contrast to the down-regulation of mitochondrial gene expression in human nasopharyngeal samples and autopsy tissues from patients with COVID-19, HIF-1α target genes, glycolysis genes, mTOR signaling genes, and genes of the ISR were up-regulated (Fig. 4). The majority of HIF-1α target genes were up-regulated in the lung, heart, kidney, and liver autopsy samples, although less so in the nasopharyngeal samples (Fig. 4A). Activation of HIF-1α not only up-regulates glycolysis but also optimizes complex IV for low oxygen tension conditions by down-regulating COX4i1, inducing LON protease to degrade COX4i1 and inducing COX4i2 (*26*). This was seen in both the human heart and nasopharyngeal samples (Fig. 4B). Expression of mTOR genes, which are essential for nutrient uptake (*39*, *51*), was up-regulated in the lung and lymph node autopsy samples and, to a lesser extent, in the nasopharyngeal samples but was markedly down-regulated in the heart autopsy samples and, to a lesser extent, in the kidney and liver autopsy samples (Fig. 4, A and C). In the nasopharyngeal, lung, and lymph node tissues, mTOR gene induction correlated with *STK11*, *AKT1*, and *AKT2* kinase genes but not with the AMP-activated protein kinase genes (*PRKAA2*, *PRKAB1*, and *PRKAG1*). By contrast, in the human heart, kidney, and liver autopsy samples, mTOR gene induction correlated with the up-regulation of *AKT3* (Fig. 4C). Whereas the up-regulation of mTOR in the nasopharyngeal and lung tissues would favor glycolysis, mTOR down-regulation in hearts, kidneys, and livers may reflect the global down-regulation of bioenergetic genes.

SARS-CoV-2 infection created an imbalance between cytosolic (fig. S3A) and mitochondrial (fig. S7) ribosomal gene expression, which could lead to the activation of the mitochondrial (UPR^{MT}) and cytosolic (UPR^{CT}) unfolded protein responses. This activation would inhibit OXPHOS and increase mROS production (*52*). Both the elevated mROS production and imbalance between cytosolic and mitochondrial ribosomal gene expression could activate the ISR pathway via the endoplasmic reticulum (ER) kinases HRI (EIF2AK1), PKR (EIF2AK2), PERK (EIF2AK3), and GCN2 (EIK2AK4) (Fig. 4A). The resulting phosphorylation of eIF2α would impair cytosolic protein synthesis and activate ATF4 and ATF5 to induce their *GDF15*, *GADD34*, *CHOP* (*37*, *38*), *SCAF1* (*39*), and *FGF21* (*51*) target genes. As predicted, the ISR was up-regulated in the nasopharyngeal samples and all of the human autopsy samples (Fig. 4, A and D), in association with *GDF15* mRNA being up-regulated in nasopharyngeal, lung, and heart tissues (Fig. 4D).

In the human nasopharyngeal samples, when viral titer was high, the *PKR* mRNA, which binds to double-stranded RNA, was strongly up-regulated along with *ATF3*, *ATF4*, *ATF5*, *CHOP*, *GADD34*, and *GDF15*, whereas *eIF2α* was strongly down-regulated. For the heart, kidney, liver, lymph node, and lung autopsy samples where the virus had been cleared, the ISR was less induced and *eIF2α* was not down-regulated. Last, the HRI kinase, which is activated by DELE1 in response to the UPR^{MT}, was down-regulated in the nasopharyngeal and heart samples, perhaps reflecting the early stage of infection in the former and the inactivation of mitochondrial function in the latter (Fig. 4, A and D).

miR-2392 induced by SARS-CoV-2 regulates mitochondrial mRNA function in human nasopharyngeal and autopsy samples

SARS-CoV-2 infection is associated with an increase in miR-2392, with the seed sequence of the induced miRNA matching the host miRNA sequence (fig. S8) (*53*, *54*). miR-2392 has been reported to enter the mitochondrion and bind to ACO2, and this complex then binds to the mtDNA $tRNA^{Gln}$ gene (*MT-TQ*) (*55*). This binding blocks the progression of the mitochondrial RNA polymerase as it transcribes the mtDNA genes of the mtDNA G-rich H strand into a polycistronic RNA (*55*).

Consistent with the proposed action of miR-2392, mtDNA transcript analysis of the human nasopharyngeal samples with high and medium viral loads revealed that the *MT-ND1* gene upstream of *MT-TQ* was up-regulated, whereas the genes downstream of *MT-TQ* were down-regulated. Moreover, the *MT-ND6* gene located on the opposite strand and transcribed from a different promoter was up-regulated (Fig. 5A). By contrast, in the human autopsy tissues in which the virus had been cleared, all of the mtDNA mRNAs were induced (Fig. 5A). miR-2392 induced by SARS-CoV-2 may also interact with the mRNAs of the nDNA mitochondrial genes. Analysis of miR-2392 seed sites among the about 1000 known nDNA mitochondrial genes (*43*, *44*) revealed that 362 mitochondrial mRNAs harbored miR-2392 binding sites (table S3). The enrichment of nDNA mitochondrial transcripts that harbored miR-2392 seeds was 3.9×10^{43} in OXPHOS genes, 1.2×10^{72} in mitochondrial biogenesis genes, and 1.2×10^{148} in mitochondrial metabolism genes (Fig. 5B, fig. S10, and table S3).

Two nDNA mitochondrial mRNAs harbored four miR-2392 binding sites: the complex I and IV assembly factor genes, *COA1*, and the fatty acid activation acyl-CoA thioesterase gene, *ACOT11*. The complex I MT-ND4 module assembly factor gene *DMAC2* had three sites. Furthermore, genes encoding OXPHOS complexes I to V, mitochondrial biogenesis, mitochondrial fusion, mitophagy, and antioxidant proteins had one or two miR-2392 sites, including the mitochondrial antiviral protein mRNA *MAVS* (fig. S9B). Some of the same OXPHOS transcripts that were up-regulated in response to SARS-CoV-2 infection harbored miR-2392 seed sites. Examples of up-regulated genes with miR-2392 sites included the complex III assembly factor *UQCC1* mRNA harboring three miR-2392 sites and *UQCC2* and *UQCC3* mRNAs with two sites (Fig. 1B).

To confirm that miR-2392 influenced mitochondrial nDNA mRNA, we transfected the cells of a three-dimensional (3D)

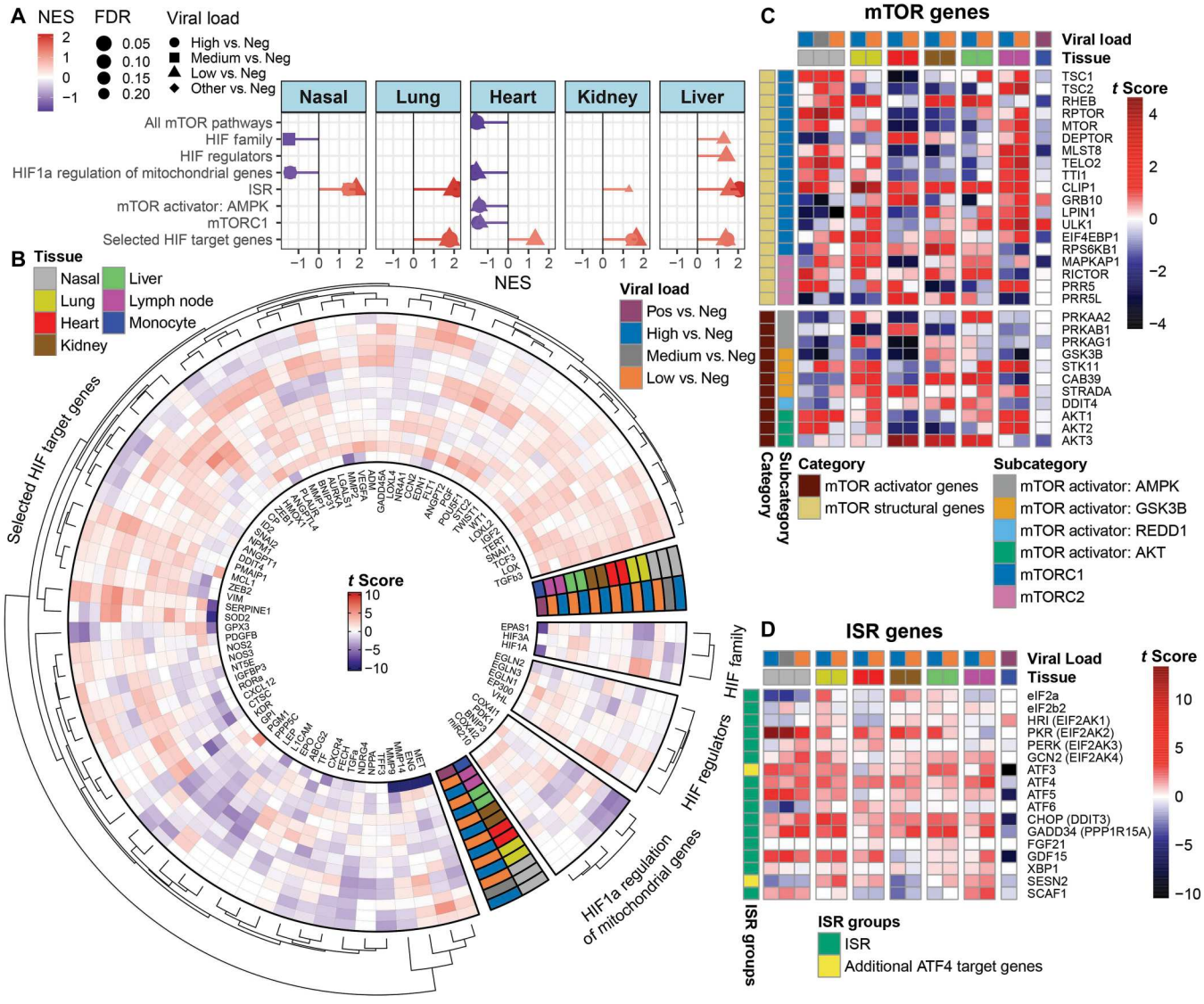

Fig. 4. HIF-1α, mTOR, and ISR pathway gene expression in nasopharyngeal and autopsy samples from patients with COVID-19. (**A**) Lollipop plots for statistically significant HIF-1α, mTOR, and integrated stress response (ISR) pathway gene sets determined by fGSEA for nasopharyngeal and autopsy (lung, heart, kidney, liver, and lymph node) samples from patients with COVID-19 were ranked by NES. (**B**) The circular heatmap displays the *t*-score statistics for HIF-1α and HIF-1α target genes in nasopharyngeal and autopsy samples that did or did not contain SARS-CoV-2 viral loads. (**C**) Heatmap displays the *t*-score statistics for mTOR genes in nasopharyngeal and autopsy samples that did or did not contain SARS-CoV-2 viral loads. (**D**) Heatmap displays the *t*-score statistics for ISR pathway genes in nasopharyngeal and autopsy samples that did or did not contain SARS-CoV-2 viral loads.

human umbilical vein endothelial cell–tissue microvascular model (HUVEC-MT) and a human neuroblastoma cell line (SH-SY5Y) with an miR-2392 mimic in vitro (Fig. 5C). In the 3D HUVEC-MT model, the miR-2392 mimic resulted in general down-regulation of OXPHOS mRNAs, up-regulation of HIF pathway genes, activation of ISR genes, and induction of *CMPK2* indicative of induction of inflammation (Fig. 5, C to E, and fig. S10, A and B). In the SH-SY5Y cells, the miR-2392 mimic strongly down-regulated specific complex I genes and induced the *LONP1* protease, the latter consistent with HIF-1α activation, although most of the ISR genes were decreased (Fig. 5, C to E, and fig. S10, A and B). The difference between the 3D HUVEC-MT cells and SH-SY5Y cells may be because of 3D HUVEC-MT cells being primarily oxidative, whereas the SH-SY5Y cells are cancerous and glycolytic (Fig. 5, F to J).

Metabolic flux in host cells in response to SARS-CoV-2 infection

To verify the metabolic effects of SARS-CoV-2 infection, we used alterations in host mRNAs to estimate the flux rates of metabolites through bioenergetics pathways in human nasopharyngeal samples and autopsy tissues from patients with COVID-19 (Fig. 6, A to D) (*56*). This analysis confirmed that the functions of the mitochondrial bioenergetics pathways and antioxidant defense pathways were suppressed in the nasopharyngeal samples and in the heart,

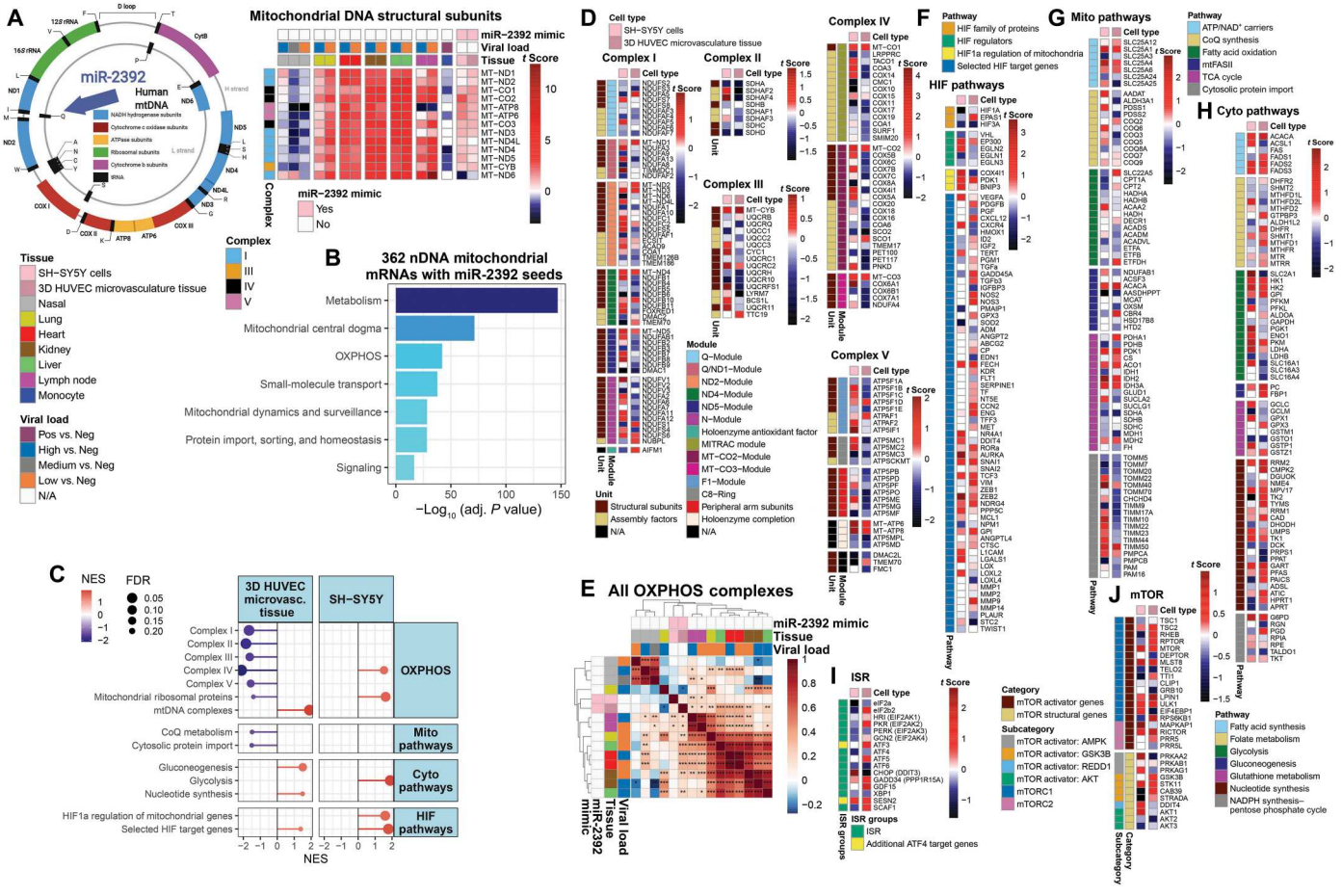

Fig. 5. SARS-CoV-2 induction of miR-2392 modulates mitochondrial transcription of mtDNA- and nDNA-encoded bioenergetic genes. (**A**) Left: Gene map of human mtDNA showing the opposing H-strand and L-strand promoters and the putative miR-2392 binding site in the *MT-TQ* $tRNA^{Gln}$ gene. (A) Right: Comparison of mtDNA transcripts (i.e., *t* scores) in nasopharyngeal and autopsy samples from patients who were COVID-19–positive or COVID-19–negative, and the effects of miR-2392 mimic treatment in 3D HUVEC-MT cells and SH-SY5Y cells compared with untreated cells. (**B**) Statistical significance or the presence of miR-2392 seed sequences in nDNA-encoded mitochondrial pathway genes is indicated by $-\log_{10}$ (adj. *P* value). (**C**) Lollipop plots for statistically significant changes in bioenergetic and metabolic pathway gene sets were determined by fGSEA for 3D HUVEC-MT tissue and SH-SY5Y cells treated with a miR-2392 mimic and were ranked by NES. (**D**) Heatmap of bioenergetic gene transcripts displays the *t*-score statistics for miR-2392 mimic–treated 3D HUVEC-MT tissue and SH-SY5Y cells. (**E**) Correlation plot of OXPHOS complex gene expression shows a close association between OXPHOS gene expression in miR-2392 mimic–treated 3D HUVEC-MT tissue and SH-SY5Y cells and that in nasopharyngeal samples from patients with COVID-19. (**F** to **J**) Heatmaps display *t*-score statistics for miR-2392 mimic–treated 3D HUVEC-MT tissue and SH-SY5Y cells for HIF-1α pathway genes (F), mitochondrial metabolic pathway genes (G), cytosolic metabolic genes (H), ISR pathway genes (I), and mTOR pathway genes (J).

kidney, liver, and lymph node autopsy tissues but were enhanced in autopsy lung samples (Fig. 6, A to D, and fig. S11).

Changes in mitochondrial gene expression during SARS-CoV-2 infection in hamsters and mice

To assess the effects of SARS-CoV-2 during the earliest stages of infection, we analyzed the transcriptional profiles of SARS-CoV-2–infected hamsters 3 days post infection (dpi) when viral RNA was at a maximum (fig. S12A). To further characterize the host transcriptional response as viral loads continued to decline, we analyzed wild-type BALB/c mice (fig. S12B) and C57BL/6 mice (fig. S12C) infected with the SARS-CoV-2 MA10 strain at 4 dpi.

In hamsters infected with SARS-CoV-2 WA strain (*57*), RNA was evaluated in the lungs, hearts, kidneys, cerebella, striata, and olfactory bulbs (Fig. 7A and fig. S13, A and B). SARS-CoV-2 viral RNA was only detected in the lungs and not in the hearts, kidneys, or brains (fig. S14). OXPHOS gene expression was minimally affected in the lungs, which suggests that this time point in hamster infection was earlier than the time point when human nasopharyngeal samples were collected. The viral RNA binding protein gene, *PKR*, was up-regulated in all hamster tissues as were the HIF-1α target genes, although variably in the striata (Fig. 7B). Individual OXPHOS mRNAs were not markedly perturbed in the hearts, lungs, kidneys, and olfactory bulbs of hamsters and neither was expression of genes for mtFASII, CoQ synthesis, protein import, TCA cycle, fatty acid oxidation, glutathione synthesis, and fatty acid synthesis. However, a subset of mitochondrial ribosomal genes was induced in the hamster hearts, lungs, and kidneys, and mild increases in expression were seen in the hearts and lungs for genes associated with folate metabolism, NADP synthesis, nucleotide metabolism, HIF-1α target genes, and ISR (Fig. 7B). In contrast to the minimal effects of acute SARS-CoV-2 infection on the

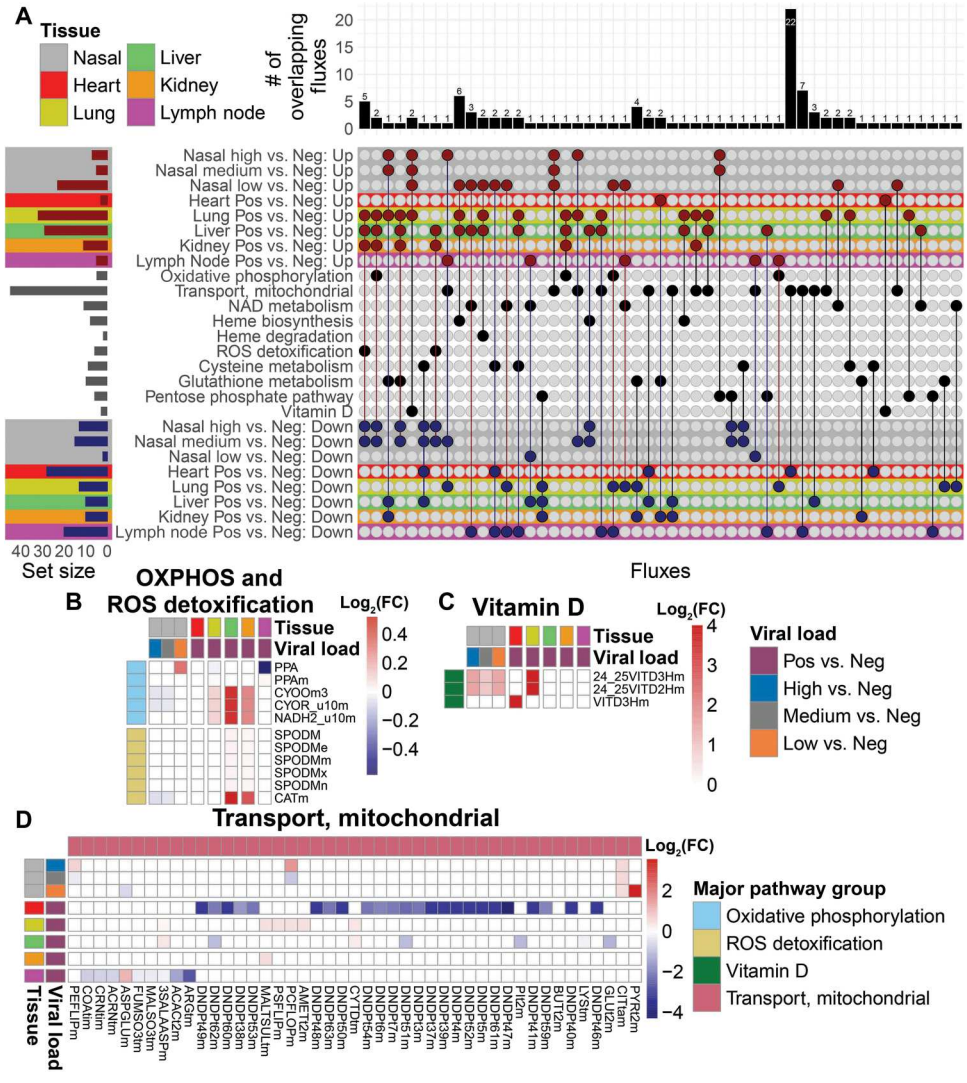

Fig. 6. Metabolic flux in nasopharyngeal and autopsy samples from patients with COVID-19. RNA-seq analysis revealed metabolic flux in nasopharyngeal and autopsy samples from patients with COVID-19. (**A**) Shown is an upset plot of the overlapping up-regulated and down-regulated metabolic fluxes from RNA-seq of nasopharyngeal and autopsy samples from patients with COVID-19. Dark red dots represent the up-regulated metabolic fluxes and dark blue dots represent the down-regulated metabolic fluxes. The bar chart at the top shows the number of overlapping metabolic fluxes for each intersection or overlap. The set size bar plot represents the total number of metabolic fluxes contained in each row. (**B** to **D**) Heatmaps show the $\log_2$ fold change in metabolic fluxes in the OXPHOS/ROS detoxification pathway (B), the vitamin D pathway (C), and mitochondrial transport pathways (D). The color bars represent the $\log_2$ fold change values, with red indicating up-regulation and blue indicating down-regulation (low but significant values may not be apparent).

hamster lungs, viscera, and olfactory bulbs, the cerebella manifested the down-regulation of OXPHOS genes, whereas the striata showed induction of OXPHOS genes (Fig. 7B). Extending this analysis (fig. S13B), the mitochondrial superoxide dismutase gene (*Sod2*) was up-regulated in the lungs, and the antioxidant *Mpv171* gene was down-regulated. In the cerebella and striata, the citrate carrier (*Slc25a1*) was down-regulated along with CoQ synthesis genes and folate metabolism genes. Consistent with early phase SARS-CoV-2 infection, the innate immune mtDNA replication gene, *Cmpk2*, was mildly up-regulated in the hearts 2.2-fold, in the lungs 2.1-fold, and in the olfactory bulbs 2.0-fold but was down-regulated in the cerebella 0.65-fold and in the striata 0.50-fold (fig. S13). Thus, early during viral infection, when SARS-CoV-2 RNA was at a peak in hamster lungs (fig. S12A) and viral polypeptides were binding to mitochondrial proteins, the virus had not yet modulated host lung or visceral mitochondrial gene transcription (Fig. 7, A and B). Although there was almost no detectable virus in the brain (fig. S14), there was differential expression of brain bioenergetic genes (Fig. 7, A and B).

The lungs of wild-type BALB/c and C57BL/6 mice infected with SARS-CoV2 MA10 and analyzed at 4 dpi showed a decline in viral titer indicative of an intermediate phase of infection (fig. S12) (*58*). Both mouse strains shared 180 up-regulated and 89 down-regulated mitochondrial genes (Fig. 8A). However, C57BL/6 mice showed variable OXPHOS gene expression (Fig. 8B) reminiscent of the human nasopharyngeal gene expression profile, whereas BALB/c mice showed robust induction of OXPHOS genes characteristic of human autopsy lung tissue (Fig. 8B), with other bioenergetic

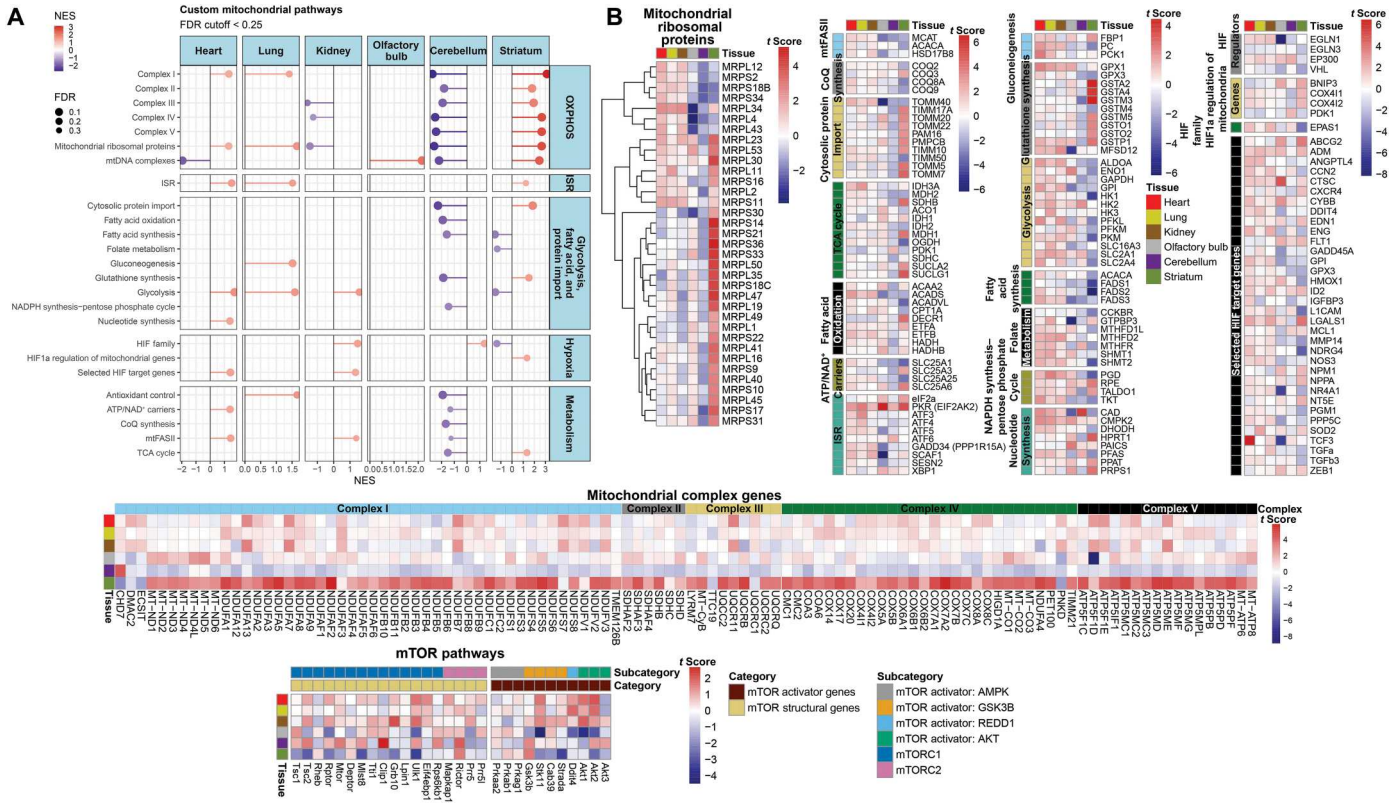

Fig. 7. Mitochondrial transcripts in SARS-CoV-2–infected hamster tissues. Shown is mitochondrial transcript analysis in SARS-CoV-2–infected hamster tissues including the hearts, lungs, kidneys, olfactory bulbs, cerebella, and striata. (**A**) Lollipop plots for statistically significant custom mitochondria and MitoPathway gene sets were determined by fGSEA and were ranked by NES. (**B**) Heatmaps display the *t*-score statistics for mitochondrial-specific genes in SARS-CoV-2–infected hamster tissues including the hearts, lungs, kidneys, olfactory bulbs, cerebella, and striata.

pathways showing similar differential pathway gene expression profiles (Fig. 8B). The mitochondrial inflammation genes, *Cmpk2* and *Acod1*, were among the top induced genes in both strains, with *Cmpk2* being induced 2.3-fold in C57BL/6 mouse lungs and 5.1-fold in BALB/c mouse lung (Fig. 8B and fig. S15) indicating robust mitochondrial activation of the innate immune response. Therefore, SARS-CoV-2 MA10 viral titers in the lungs of C57BL/6 and BALB/c mice at 4 dpi fall between the SARS-CoV-2 viral titers of human nasopharyngeal samples and human lung autopsy samples. Specifically, the BALB/c lung viral titers declined further than those of C57BL/6 mice, placing the order of progressive viral loss as hamster lungs with peak viral titer, human nasopharyngeal samples with high viral titers, C57BL/6 mouse lungs with partially reduced viral titers and BALB/c mouse lungs with a further reduction in viral titer, and, lastly, human autopsy lung tissue with no detectable virus.

DISCUSSION

Upon SARS-CoV-2 infection of host cells, the viral copy number increases unchecked until the innate immune system is engaged, after which the viral copies progressively decline until the virus is eliminated. By quantifying SARS-CoV-2 RNA copies, we ordered multiple human and rodent SARS-CoV-2 datasets to encompass the entire course of COVID-19 progression (figs. S16 and S17). Given that SARS-CoV-2 viral RNA is evaluated by RNA-cDNA sequencing of cellular cDNA, we were able to correlate changes in SARS-CoV-2 RNA with changes in the expression of host bioenergetic genes, with special emphasis on the genes of the mitochondrion, glycolysis, and allied processes. In this way, we were able to define the host bioenergetic changes across the full course of COVID-19 progression. The initial peak viral copy number in hamster lung represents the earliest stage of SARS-CoV-2 infection. This was followed by human nasopharyngeal samples from patients with high, medium, or low viral RNA, which represented the progression of viral decline associated with the activation of host antiviral immune defenses. The effects of declining viral load were further evaluated in SARS-CoV-2 MA10–infected C57BL/6 mice and BALB/c mice, with C57BL/6 mouse viral load having declined proportionally less than that of BALB/c mice. Last, human autopsy tissue samples from patients who had died from COVID-19 were placed at the end of COVID-19 progression because the entire autopsy tissues were devoid of viral RNA.

At the earliest stage of SARS-CoV-2 infection, when viral RNA first peaked in hamster lungs and viral RNA was absent in the hearts, kidneys, and brains, ISR *PKR* mRNA was beginning to increase as was *Cmpk2* mRNA, indicating the activation of inflammasomes with stimulation of mtDNA replication. At this stage, bioenergetic gene expression was minimally affected in the lungs and viscera. Unexpectedly, however, mitochondrial gene expression was down-regulated in the cerebella and strongly induced in the striata of the hamster brains. The absence of viral effects on lung

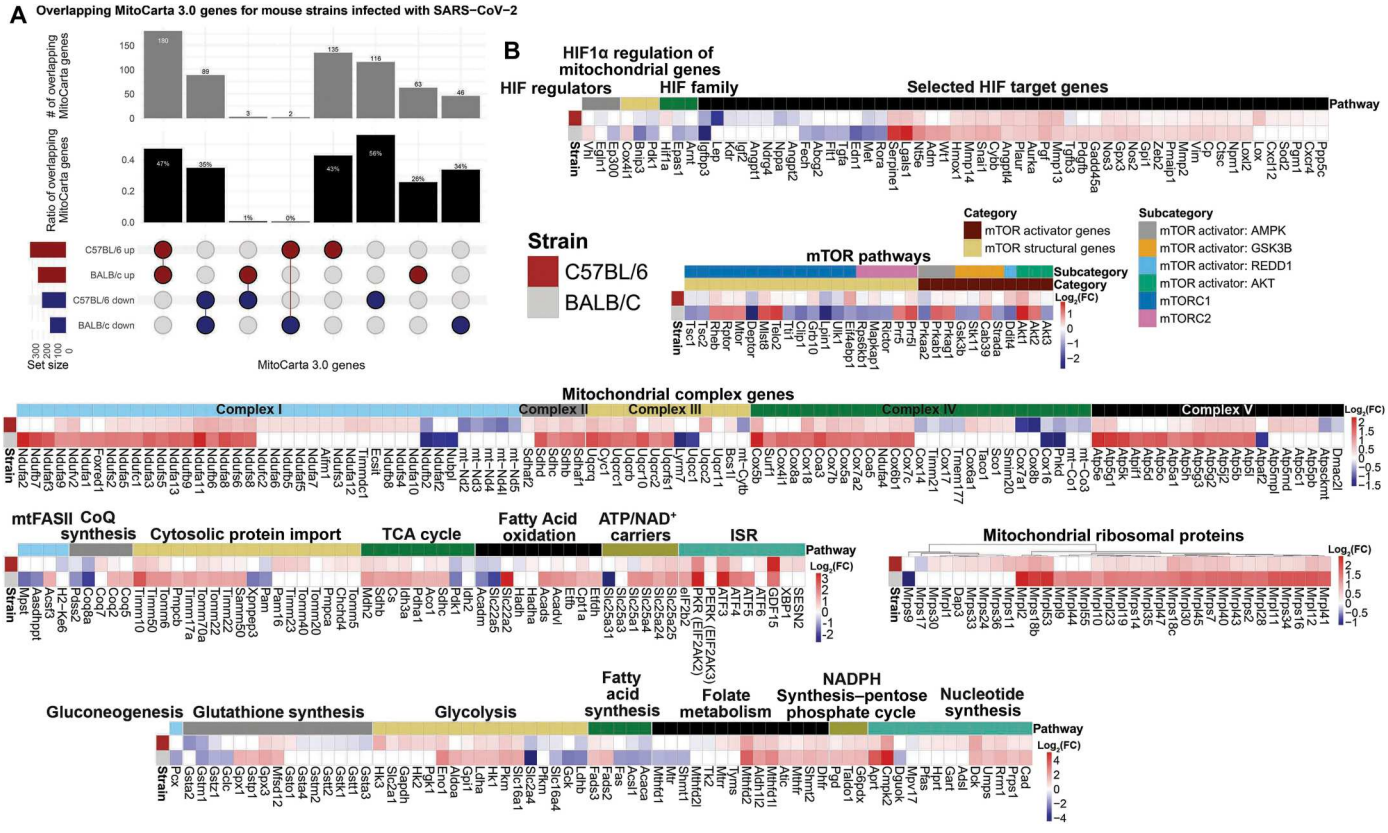

Fig. 8. Mitochondrial transcripts in SARS-CoV-2–infected mouse lung tissues. (**A**) Shown is an upset plot of the overlapping MitoCarta genes when comparing lungs from SARS-CoV-2–infected wild-type BALB/c mice and C57BL/6 mice. (**B**) Heatmaps display the *t*-score statistics for mitochondrial-specific genes in SARS-CoV-2–infected BALB/c and C57BL/6 mouse lungs.

mitochondrial gene expression where viral RNA was high compared with robust changes in mitochondrial gene expression in the brain where viral RNA was absent raised the possibility that modulation of energy metabolism in distant tissues might be because of ISR activation producing diffusible factors such as GDF15, which could potentially modulate mitochondrial function in tissues far from the initial site of infection.

Whereas pulmonary mitochondrial gene transcription was not affected at the initial stage of hamster infection, SARS-CoV-2 was actively synthesizing viral proteins that bind to a wide array of mitochondrial proteins, leading to the inhibition of mitochondrial function (*13*–*15*). OXPHOS inhibition is critical for viral propagation because it shifts carbon substrates away from terminal oxidation to glycolysis, where the substrates can be used to generate lipids and nucleic acids for viral propagation. Stimulation of glycolysis is achieved by viral inhibition of OXPHOS and elaboration of Nsp5 to bind to glutathione peroxidase 1, both of which stimulate mROS production. Increased mROS then stabilizes HIF-1α, which up-regulates glycolytic gene expression.

In the human nasopharyngeal samples, the three different amounts of SARS-CoV-2 RNA may reflect the progression of COVID-19 from earlier pulmonary infection with high viral titers to later pulmonary infection with low viral titers. At the highest nasopharyngeal viral RNA load, the expression of mitochondrial OXPHOS genes and associated bioenergetic genes was markedly down-regulated, but the inhibition of OXPHOS genes progressively declined as the viral load declined. The host cells compensated for the viral inhibition of host mitochondrial function caused by viral protein binding to mitochondrial proteins, by up-regulating mitochondrial biogenesis. To sustain OXPHOS inhibition and glycolysis stimulation, the virus next inhibited host mitochondrial gene transcription. Thus, in the human nasopharyngeal samples with high and medium viral loads, we observed marked down-regulation of the mitochondrial transcripts of specific clusters of structural or assembly genes required for the biogenesis of individual OXPHOS complex subassembly modules. The virus only needs to block the synthesis of one or more subassembly modules to inactivate the entire OXPHOS complex. The host attempts to compensate by up-regulating mitochondrial gene transcription, but only those structural and assembly genes not specifically blocked by the virus can be induced.

To inhibit nDNA-encoded mitochondrial gene transcripts, the virus produces a number of polypeptides that interfere with nuclear functions, such as Nsp12, which binds to CREB (cyclic adenosine 3′,5′-monophosphate response element–binding protein); Nsp5, which binds to HDAC2; and Orf8, which is located at the nuclear envelope (*13*, *59*, *60*). The virus also induces miR-2392 (*53*) which, in the high and medium viral load nasopharyngeal samples, inhibited mtDNA H-strand transcription, blocking the synthesis of 11 of the 13 mtDNA polypeptides. miR-2392 also binds to more than 360 nDNA-encoded mitochondrial mRNAs, potentially blocking their translation and further

inhibiting OXPHOS biogenesis. Thus, SARS-CoV-2 maintained OXPHOS inhibition and glycolytic induction by inhibition of mitochondrial protein functions, selective disruption of OXPHOS module transcription, miRNA-mediated inhibition of mtDNA transcription, and miRNA-mediated inhibition of nDNA mitochondria mRNA translation.

The host innate immune response becomes fully activated upon induction of the ISR and *CMPK2*-mediated mtDNA activation of the inflammasome. Impaired mitochondrial protein synthesis creates an imbalance in nDNA and mtDNA proteins, activating UPR^{MT} and UPR^{CT}, which activate the ISR. The ISR shuts down cytosolic protein synthesis, activates mitochondrial single-carbon metabolism, and elaborates mitokine production including GDF15. SARS-CoV-2 viroporins E and Orf3a permit the influx of Ca^{++} into host cells, which is taken up by the mitochondrion to activate the TCA cycle. This generates excess NADH, which overloads the electron transport chain increasing mROS production. Increased mROS together with the *CMPK2* activation of mtDNA synthesis generates Ox-mtDNA, which is released through the mitochondrial permeability transition pore and binds to the inflammasome to generate interleukin-1β. Unoxidized mtDNA released into the cytoplasm likely binds to cyclic GMP-AMP synthase to drive the interferon response (*IFI27*, *ACOD1/IRG1*, and *MAVS*) (*61*). The continued activation of the ISR and the production of GDF15 or other mitokines may affect changes in mitochondrial gene expression in brain cells not infected with SARS-CoV-2.

Relative to peak viral load, the viral RNA copy number in the SARS-CoV-2 MA10–infected C57BL/6 and BALB/c mouse lungs had declined at the time we chose for bioenergetic gene transcription analysis. The action of the host innate immune system to induce decreases in viral RNA was reflected by the induction of the *Cmpk2* mRNA in the lungs of both mouse strains. The C57BL/6 mouse viral load had decreased less than that of BALB/c mice, and so we predicted that these infected mice represented an earlier stage in COVID-19 progression. Consequently, the variable OXPHOS gene expression observed in the infected C57BL/6 mice may reflect a slow reactivation of mitochondrial gene expression as was noted in the human nasopharyngeal samples as viral propagation declined. In the BALB/c mouse lungs, the viral copy number had declined to a greater extent than in the C57BL/6 mouse lungs, further mitigating the viral inhibition of mitochondrial gene transcription. The loss of viral inhibition resulted in the robust up-regulation of OXPHOS genes in the BALB/c mouse lungs.

Last, in the human autopsy tissues, the viral RNA had been eliminated, which was consistent with the systemic activation of the ISR and the induction of *CMPK2* in the heart. In the autopsy lung samples, the absence of the virus was associated with the robust up-regulation of nDNA mitochondrial OXPHOS gene expression. In all autopsy tissues, mtDNA transcription was strongly induced, presumably reflecting the decline in miR-2392 as the virus was cleared. However, the strong inhibition of nDNA transcription in the hearts was not reversed nor was the partial inhibition of OXPHOS in the kidneys, livers, and lymph nodes. It is unclear why the removal of the virus did not reverse the OXPHOS inhibition in the viscera, but the continued inhibition of mitochondrial gene expression in the hearts, kidneys, and livers likely contributed to lethality in these COVID-19 cases. For individuals in whom visceral nDNA mitochondrial gene transcription was partially reactivated and who survived severe COVID-19, the sustained partial inhibition of OXPHOS potentially could be a contributor to long COVID, with chronic inhibition of mitochondrial bioenergetics contributing to the chronic malaise associated with COVID-19. ISR activation and *Cmpk2*-mediated inflammasome activation could contribute to systemic inflammatory symptoms and perhaps cytokine storm. The irreversible inhibition of visceral mitochondrial transcription could also contribute to the multisystem symptoms of long COVID.

This study has a number of limitations. First, some of the clinical components of the study were designed retrospectively; thus, COVID-19 groups and control groups were not matched for demographic variables, comorbidities, or in-hospital treatments. In addition, there was limited availability of human samples from all organs across the entire course of SARS-CoV-2 infection. This necessitated the inclusion of rodent data from which the requisite organs could be collected and analyzed, with disease progression determined by relative changes in viral RNA throughout the course of human and rodent infections.

Therapies that enhance mitochondrial function, minimize mROS, and block mtDNA release potentially could reduce the more severe symptoms of acute SARS-CoV-2 infection and mitigate the symptoms of long COVID. In support of this hypothesis, treatment of SARS-CoV-2–infected monocytes with the antioxidants NAC and MitoQ reduced mROS production, HIF-1α protein, pro-inflammatory mRNA, and viral loads (*22*). Treatment with the mTOR inhibitor, rapamycin, also impairs SARS-CoV-2 propagation (*30*). Activation of mitochondrial biogenesis with bezafibrate (*62*) or neutralization of miR-2392 (*53*) might impair the shift from OXPHOS to glycolysis and impede SARS-CoV-2 replication and propagation. Thus, knowledge of the effects of SARS-CoV-2 on host bioenergetics suggests alternative approaches to treating both acute and chronic COVID-19.

MATERIALS AND METHODS

Study design

We set out to determine the effects of SARS-CoV-2 infection on mitochondrial function in tissue samples from patients with COVID-19 compared with uninfected individuals. We calculated the relative expression of host genes in RNA sequencing (RNA-seq) data from 216 COVID-19–positive and 519 COVID-19–negative human nasopharyngeal samples, and from heart, lung, liver, kidney, and lymph node autopsy tissues from 35 or 36 COVID-19–positive and 5 to 8 COVID-19–negative patients. We then compared host gene expression in tissue samples from SARS-CoV-2–infected and uninfected control individuals using our curated set of cellular bioenergetics genes (table S2) plus the MitoCarta and MitoPathway gene lists (*43*, *44*).

We also conducted studies in 6- to 7-week-old male golden Syrian hamsters (*Mesocricetus auratus*; Charles River Laboratories) infected with the USA-WA1/2020 strain of SARS-CoV-2 (*57*) and 16-week-old female C57BL/6 mice and 10- to 12-week-old female BALB/c mice infected with the mouse-adapted MA10 strain of SARS-CoV-2 (*58*). All animal experiments were conducted using approved standard operating procedures and safety conditions for SARS-CoV-2 in BSL3 facilities following the safety requirements outlined in the Biosafety in Microbiological and Biomedical Laboratories, sixth edition. Protocols were approved by the Institutional Animal Care and Use Committee at Icahn School of Medicine,

Mount Sinai, NY (*57*) and University of North Carolina (UNC), Chapel Hill (*58*).

For all experiments, the preprocessing steps were blinded until the higher-order analysis. No outliers or data were excluded from any of the analyses.

Human nasopharyngeal swab sample collection for RNA-seq analysis

Nasopharyngeal specimens were collected from 216 COVID-19–positive and 519 COVID-19–negative patients. We also included 17 positive (Vero E6 cells) and 33 negative (buffer) controls using BD Universal Vial Transport Media System (Becton Dickinson and Company). Total nucleic acid was extracted using the automated QIAsymphony and the DSP Virus/Pathogen Mini Kit (Qiagen) as described (*42*). DESeq2 (*63*) was used to generate the differential gene expression data.

Human autopsy tissue collection for RNA-seq analysis

Autopsy heart, kidney, liver, lymph node, and lung samples were collected from 35 to 36 patients and five to eight controls with the consent of the next of kin and permission for retention and research use. Samples were placed directly into TRIzol, homogenized, and then snap-frozen in liquid nitrogen (*64*).

The subdivision of autopsy cases into "high viral load" and "low viral load" on "admission" was determined from the nasopharyngeal swab samples from patients with COVID-19 at the time of infection and hospital visit. The viral loads were assessed with a quantitative reverse transcription polymerase chain reaction (qRT-PCR) cycle threshold (Ct) value of SARS-CoV-2 primers, with Ct of less than or equal to 18 being assigned to high viral load and Ct between 18 and 40 being assigned to low viral load. Ct values above 40 were classified as negative.

RNA sequencing and analysis

Autopsy and nasopharyngeal samples were placed in TRIzol, homogenized, and frozen. RNA-seq libraries were prepared by the New York Genome Center using the KAPA Hyper Library Preparation Kit + RiboErase, HMR (Roche). rRNA-depleted samples underwent first- and second-strand cDNA synthesis followed by adenylation and ligation of unique dual-indexed adapters. Libraries were amplified using 12 cycles of PCR and cleaned up by magnetic bead purification, quantified using PicoGreen (Life Technologies) or Qubit Fluorometer (Invitrogen) and Fragment Analyzer (Advanced Analytics), and sequenced on a NovaSeq 6000 sequencer (v1 chemistry) with 2 × 150 base pairs (bp) targeting 60 M reads per sample. RNA-seq data were processed as described by Butler *et al.* (*42*) and Park *et al.* (*64*).

SARS-CoV-2 MA10 infection of mice and RNA-seq on mouse lung tissues

The mice were housed in the UNC ABSL3 facility on a 12:12 light cycle using autoclaved cages (Tecniplast, EM500), irradiated Bed-o-Cob (ScottPharma, Bed-o-Cob 4RB), ad libitum irradiated chow (LabDiet, PicoLab Select Rodent 50 IF/6F 5V5R), and autoclaved water bottles. Animals used in this study included 16-week-old female C57BL/6 J (B6) (Jackson Laboratory, stock 000664) or 10- to 12-week-old BALB/cAnNHsd (BALB/c) (Envigo order code 047) mice, purchased directly from vendors.

Mice were infected after light sedation, using ketamine (50 mg/kg) and xylazine (15 mg/kg), by intranasal inoculation with 10^4 pfu SARS-CoV-2 MA10 (*52*) diluted in 50 μl of phosphate-buffered saline (PBS) or PBS alone (mock infection). Blinded treatment groups for mice were used throughout the study to limit investigator subjectivity. Mice were euthanized by an overdose of isoflurane anesthetic, and lung tissues were collected for subsequent processing.

RNA from inferior mouse lung lobes was extracted using TRIzol reagent (Thermo Fisher Scientific), followed by overnight precipitation at −20°C, and quantified using a NanoDrop spectrophotometer (Thermo Fisher Scientific). rRNA from 1000 ng of total extracted RNA was depleted using a NEBNext rRNA Depletion Kit (Human/Mouse/Rat; New England Biolabs Inc.). The remaining RNA was used to produce the sequencing libraries using the NEBNext Ultra II Directional RNA Library Prep Kit for Illumina (New England Biolabs Inc.) with AMPure XP (Beckman Coulter Life Sciences) for all bead cleanup steps. The libraries were sequenced on a NovaSeq 6000 System, using a NovaSeq 6000 SP Reagent Kit v1.5 (Illumina).

Analysis of RNA-seq data from SARS-CoV-2–infected mouse tissues

The RNA-seq reads were aligned to the *Mus musculus* BALB/c or C57Bl/6 genome (v1.100) and the SARS-CoV-2 MA10 genome (MT952602) using the CLC Genomics Workbench v20.0 (https://digitalinsights.qiagen.com/) with the RNA-seq and small RNA analysis pipeline and the RNA-seq analysis module with all standard settings; the read counts were then calculated. The fold change and adjusted *P* values were calculated and used for all downstream analyses in a similar manner to those for the human autopsy data.

SARS-CoV-2 WA infection of hamsters and RNA-seq on hamster tissues

The generation and processing of hamster tissues and RNA samples were performed as described in (*57*).

Transfection of 3D HUVEC tissue with miR-2392 mimics

Mature human 3D microvascular tissues were grown by seeding HUVECs (Lonza, catalog no. CC-2519) into a collagen/Matrigel mixture as described previously (*53*). Briefly, HUVECs were first grown in EGM endothelial cell growth medium (catalog no. CC-3124), then cells (1×10^6/ml) were embedded into a collagen/Matrigel mixture (catalog nos. 354236 and 356230). Microvessels were grown in EGM-2 endothelial cell growth medium (catalog no. CC-3162) plus 50 nM phorbol 12-myristate 13-acetate (catalog no. 524400) for 7 days to form tubular microvessels before irradiation.

These tissue models were used to study vascular changes associated with miR-2392 mimics. The 3D HUVEC tissues were incubated according to the manufacturer's instructions with the miR-2392 mimics or control lentivirus particles (multiplicity of infection 1) for 48 hours. Specifically, we used the shMIMIC Lentiviral microRNA hsa-miR-2392 hCMV-TurboGFP UHT kit with the SMARTvector Non-targeting hCMV-TurboGFP Control Particles for the control vehicle transfection (Horizon Discovery Biosciences Limited, catalog nos. VSH7357 and VSC10236). The tissue constructs used for miR-2392 mimics were dissolved in TRIzol (Thermo Fisher Scientific, catalog no. 15596026) 48 hours after transfection, without any fixation or homogenization. Cell

culture, RNA analysis, and data processing of miR-2392 mimic experiments in SH-SY5Y cells and RNA-seq were conducted as described previously (*60*).

RNA-seq of 3D HUVEC-MT tissue transfected with miR-2392 mimics

RNA was extracted using the RNeasy Universal kit (Qiagen, Valencia, CA). Gel matrix cryotubes containing the cells of interest were taken out of −80°C, and 1 ml of QIAzol reagent was added to the tubes. Each sample contained 300 to 800 μl of gel matrix and about 500,000 cells. Whereas the gel matrix was thawed in QIAzol, the solution was pipetted and vortexed until fully dissolved. The lysate was passed through a QIAshredder column (Qiagen, Valencia, CA) to further homogenize the cells. One hundred microliters of genomic DNA eliminator solution was added. The resulting lysate from each sample was then used to isolate and purify RNA following the manufacturer's protocol. RNA was eluted in 30 to 50 μl of ribonuclease-free H_2O. The concentration of all RNA samples was measured using Qubit 3.0 Fluorometer (Thermo Fisher Scientific, Waltham, MA) with Qubit RNA BR kit after SOP 4.1-RNA/DNA/miRNA/cDNA quantification using a Qubit Fluorimeter. RNA quality was assessed using the Agilent 4200 TapeStation with the Agilent RNA ScreenTape (Agilent Technologies, Santa Clara, CA).

Ribosomal RNA depletion and library preparation were done with Illumina TruSeq Stranded Total RNA Library Prep Gold (Illumina Inc., San Diego, CA). Input RNA was about 500 ng with RNA integrity number (RIN) > 6.5 (average RIN of 8.7). Index adapters used were at 1.5 μM (IDT, 384-well xGen Dual Index UMI Adapters). Fifteen cycles of PCR were performed. Library fragment size was assessed using an Agilent 4200 TapeStation System with D1000 DNA ScreenTape (Agilent Technologies, Santa Clara, CA) after GeneLab SOP 6.3 quality analysis of sequencing libraries using a 4200 TapeStation System with D1000 reagent kit. Pooled library concentration was measured by a Qubit 4 Fluorometer (Thermo Fisher Scientific, Waltham, MA) after SOP 4.1-RNA/DNA/miRNA/cDNA quantification using a Qubit Fluorimeter. Library quality assessment was performed on an iSeq100 (Illumina, San Diego, CA).

RNA-seq was performed by GeneLab Sample Processing Lab on an Illumina NovaSeq 6000. Sequencing was set up as follows: Read 1: 151 bp, Index1: 17 bp (8 bp index + 9 bp UMI), Index 2: 8 bp, Read 2: 151 bp. PhiX was included as an internal control and to increase library diversity. The protocol followed is SOP 7.1-Setting up NovaSeq 6000 and iSeq 100 Sequencers.

Raw fastq files were assessed for % rRNA using HTStream SeqScreener (version 1.3.2) and filtered using Trim Galore! (version 0.6.7) powered by Cutadapt (version 3.7). Raw and trimmed FASTq file quality was evaluated with FastQC (version 0.11.9), and MultiQC (version 1.12) was used to generate MultiQC reports. *Homo sapiens* STAR and RSEM references were built using STAR (version 2.7.10a) and RSEM (version 1.3.1), respectively, Ensembl release 101, genome version GRCh38 (Homo_sapiens.GRCh38.dna.primary_assembly.fa) concatenated with ERCC92.fa from Thermo Fisher Scientific (https://assets.thermofisher.com/TFS-Assets/LSG/manuals/ERCC92.zip), and the following GTF annotation file: *Homo sapiens*.GRCh38.101.gtf concatenated with the ERCC92.gtf file from Thermo Fisher Scientific (https://assets.thermofisher.com/TFS-Assets/LSG/manuals/ERCC92.zip). Trimmed reads were aligned to the *H. sapiens* + ERCC STAR reference with STAR (version 2.7.10a), aligned reads were assessed for strandedness using RSeQC Infer Experiment (version 4.0.0), and then aligned reads from all samples were quantified using RSEM (version 1.3.1), with strandedness set to forward. Quantification data were imported to R (version 4.1.2) with tximport (version 1.22.0) and normalized with DESeq2 (version 1.34.0) (*63*) median of ratios method. Differential expression analysis was performed in R (version 4.1.2) using DESeq2 (version 1.34.0); all groups were compared using the Wald test, and the likelihood ratio test was used to generate the *F*-statistic *P* value. Gene annotations were assigned using the following Bioconductor and annotation packages: STRINGdb (v2.8.4), PANTHER.db (v1.0.11), and org.Hs.eg.db (v3.15.0). All other analysis was similar to what is described for the other RNA-seq data.

miR-2392 seed distribution in nDNA mitochondrial gene mRNAs

We obtained all human mitochondrial genes from the Broad Institute MitoCarta database (www.broadinstitute.org/mitocarta/mitocarta30-inventory-mammalian-mitochondrial-proteins-and-pathways) on 17 May 2022 (*43*, *44*). The unique genes were analyzed using the Target Mining function of the tool miRwalk version 3, which provided an advanced search option for several miRNAs or gene targets. For this project, we mined all human mitochondrial genes and filtered those that were targeted by hsa-miR-239. The resulting human mitochondrial genes were categorized by their function pathways. The presence of different splicing isoforms overestimated the number of different miRNA targets over the 3′ untranslated region of the same transcriptional unit; therefore, we filtered accordingly and visualized the nonredundant target numbers in a radial hierarchical map.

Proteomic and transcriptomic analysis of human blood and nasopharyngeal samples, and of CaCo-2 cells

Transcriptomic and proteomic changes in paired blood and nasopharyngeal samples from patients with COVID-19 were obtained from the published data (*47*). Mass spectrometry–based proteomic data for CaCo-2 cells 24 hours after infection with SARS-CoV-2 were obtained from the same publication (*47*). Two-dimensional annotation enrichment for RNA-seq and proteomics data was performed using Perseus 1.6.14.0 for proteomic and transcriptomic analysis of mitochondrial genes (*65*, *66*) (www.nature.com/articles/nmeth.3901; https://bmcbioinformatics.biomedcentral.com/articles/10.1186/1471-2105-13-S16-S12).

Whole blood transcriptome data and plasma proteome data were downloaded from the COVIDome Explorer Researcher Portal (*66*). The following filters were used for transcriptome data: category, "Effect of COVID-19 status"; platform, "Blood"; statistical test, "Student's t-test"; adjustment method, "none"; sex, "male" and "female"; age group, "All". Similar filters were used for proteome data: category, "Effect of COVID-19 status"; platform, "SOMAscan"; statistical test, "Student's t-test"; adjustment method, "none"; sex, "male" and "female"; age group, "All." Mitochondrial genes were analyzed at both transcriptome and proteome levels, and we visualized the data using RStudio Desktop 1.3.1093, ggplot2 version 3.3.2, and ggrepel version 0.8.2 ggrepel.

Analysis of human monocyte RNA-seq data

The monocyte COVID-19 RNA-seq data, published under accession number GSE159678 (*48*), were downloaded from the National Library of Medicine's Sequence Read Archive, and gene expression was quantified using Salmon's selective alignment approach (*67*). The RNA-seq processing pipeline was implemented using pyrpipe (*68*) (https://github.com/urmi-21/pyrpipe/tree/master/case_studies/Covid_RNA-Seq). Exploratory data analysis and differential expression analysis were performed using MetaOmGraph (*69*).

Analysis combining human autopsy and nasopharyngeal sample RNA-seq data

To combine the results from the autopsy and nasopharyngeal swab RNA-seq data, we used the *t*-score values from the DESeq2 analysis. Heatmaps were displayed using pheatmap (version 1.0.12). Circular heatmaps were produced in R (version 4.1.0), using the Complex Heatmap (*70*) (version 2.9.4) and circlize (*71*) (version 0.4.12) packages.

Enrichment analysis of miRNA gene targets in human mitochondrial pathways

To associate miRNA gene targets with human mitochondrial pathways, we calculated *P* values using the Fisher's exact test for each set of pathway terms in the Human MitoCarta 3.0 hierarchy (*44*). We adjusted the *P* values using the Benjamini-Hochberg method to keep the overall significance below 0.05. The Human MitoCarta pathway has three levels in the hierarchy. The first level has seven pathway categories, the second level has 39, and the third level has 103.

Metabolic modeling and statistical analyses

We simulated the optimal fluxes of each metabolic reaction for each RNA-seq sample, using an adjusted version of a context-specific constraint-based metabolic modeling method (*51*). We constructed a context-specific genome-scale metabolic model for each RNA-seq sample by subsetting metabolic reactions in the Recon1 metabolic model (*72*) using CORDA and cobrapy (*73*) based on the RNA-seq profile expression of genes associated with each metabolic reaction. When applying CORDA, we assigned a high expression confidence score of 3 to the top 35% of highest expressed genes, a medium confidence score of 2 to the 35 to 85% of highest expressed genes, and a low confidence score of 1 to 85 to 100% of highest expressed genes to minimize the SD of flux levels across samples from each group for all groups. In addition, we manually activated the following essential pathways that were considered to be necessary for the model stability because these essential pathways may not be properly activated based on RNA-seq data alone: "Oxidative phosphorylation," "Citric acid cycle," "Glycolysis/gluconeogenesis," "CoA biosynthesis," "CoA catabolism," "NAD metabolism," "Fatty acid metabolism," "Fatty acid activation,""Fatty acid elongation," "Fatty acid oxidation," "ROS detoxification," and "Biomass and maintenance functions." On each context-specific genome-scale metabolic model, we applied flux balance analysis (FBA) with each reaction as the objective to optimize the flux of the objective reaction. The linear programming optimization problems were solved by Gurobi solver (Gurobi Optimization, LLC, 2020) with the reference manual at www.gurobi.com. All modeling procedures were implemented within a Jupyter-Notebook 6.1.5 using Python 3.7.7 (84). Whereas gene expression was applied to the modeling procedure by each RNA-seq sample, all other parameters were maintained identically for all RNA-seq samples. The modeling procedure reported the outcome as the FBA-generated optimal flux of all available reactions of each context-specific metabolic model constructed from each RNA-seq sample, and the optimal flux was analyzed as variables for comparison between grouped cohorts as discussed in the text. Given that it is impossible to presume variance or normality of flux distributions within and between cohort groups, a nonparametric Van der Waerden (VdW) test was applied to compare groupwise flux using the R matrixTests package (v. 0.1.9). Some pathways were chosen on the basis of mitochondria-associated connection or COVID-19–associated peculiarity and selected reactions with significant $P < 0.05$.

Gene set enrichment analysis

For pathway analysis, we used fast gene set enrichment analysis (fGSEA) (*67*). Pathway analysis was done using custom-made gene set files from either MitoPathway or the genes that we curated (available in table S2). Using fGSEA, all samples were compared with controls, and the ranked list of genes was defined by the *t*-score statistics. The statistical significance was determined by 1000 permutations of the gene sets (*74*).

Statistical analysis

The statistics for all the analyses either included the *P* values or adjusted *P* values (i.e., FDR). For the RNA-seq data, the statistics for the differential expression analysis were calculated with adjusted $P < 0.05$. The values for both human and hamster RNA-seq data are shown as *t* scores and for mouse RNA-seq data as $\log_2$ (fold change). All GSEA analysis statistics are shown as FDR < 0.25, and all QLattice data are shown as associated *P* values with Pearson's correlation scores.

Supplementary Materials

This PDF file includes:
Figs. S1 to S17
Tables S1 and S3

Other Supplementary Material for this manuscript includes the following:
Table S2
MDAR Reproducibility Checklist

REFERENCES AND NOTES

1. J. Saleh, C. Peyssonnaux, K. K. Singh, M. Edeas, Mitochondria and microbiota dysfunction in COVID-19 pathogenesis. *Mitochondrion* **54**, 1–7 (2020).
2. K. K. Singh, G. Chaubey, J. Y. Chen, P. Suravajhala, Decoding SARS-CoV-2 hijacking of host mitochondria in COVID-19 pathogenesis. *Am. J. Physiol. Cell Physiol.* **319**, C258–C267 (2020).
3. D. A. Jamison Jr., S. A. Narayanan, N. S. Trovão, J. W. Guarnieri, M. J. Topper, P. M. Moraes-Vieira, V. Zaksas, K. K. Singh, E. S. Wurtele, A. Beheshti, A comprehensive SARS-CoV-2 and COVID-19 review, Part 1: Intracellular overdrive for SARS-CoV-2 infection. *Eur. J. Hum. Genet.* **30**, 889–898 (2022).
4. K. Ramachandran, S. Maity, A. R. Muthukumar, S. Kandala, D. Tomar, T. M. Abd el-Aziz, C. Allen, Y. Sun, M. Venkatesan, T. R. Madaris, K. Chiem, R. Truitt, N. Vishnu, G. Aune, A. Anderson, L. Martinez-Sobrido, W. Yang, J. D. Stockand, B. B. Singh, S. Srikantan, W. B. Reeves, M. Madesh, SARS-CoV-2 infection enhances mitochondrial PTP complex activity to perturb cardiac energetics. *iScience* **25**, 103722 (2022).
5. A. P. West, G. S. Shadel, Mitochondrial DNA in innate immune responses and inflammatory pathology. *Nat. Rev. Immunol.* **17**, 363–375 (2017).

6. Z. Zhong, S. Liang, E. Sanchez-Lopez, F. He, S. Shalapour, X. J. Lin, J. Wong, S. Ding, E. Seki, B. Schnabl, A. L. Hevener, H. B. Greenberg, T. Kisseleva, M. Karin, New mitochondrial DNA synthesis enables NLRP3 inflammasome activation. *Nature* **560**, 198–203 (2018).
7. P. Wang, R. Luo, M. Zhang, Y. Wang, T. Song, T. Tao, Z. Li, L. Jin, H. Zheng, W. Chen, M. Zhao, Y. Zheng, J. Qin, A cross-talk between epithelium and endothelium mediates human alveolar-capillary injury during SARS-CoV-2 infection. *Cell Death Dis.* **11**, 1042 (2020).
8. M. Cortese, J. Y. Lee, B. Cerikan, C. J. Neufeldt, V. M. J. Oorschot, S. Köhrer, J. Hennies, N. L. Schieber, P. Ronchi, G. Mizzon, I. Romero-Brey, R. Santarella-Mellwig, M. Schorb, M. Boermel, K. Mocaer, M. S. Beckwith, R. M. Templin, V. Gross, C. Pape, C. Tischer, J. Frankish, N. K. Horvat, V. Laketa, M. Stanifer, S. Boulant, A. Ruggieri, L. Chatel-Chaix, Y. Schwab, R. Bartenschlager, Integrative imaging reveals SARS-CoV-2-induced reshaping of subcellular morphologies. *Cell Host Microbe* **28**, 853–866.e5 (2020).
9. R. Nardacci, F. Colavita, C. Castilletti, D. Lapa, G. Matusali, S. Meschi, F. del Nonno, D. Colombo, M. R. Capobianchi, A. Zumla, G. Ippolito, M. Piacentini, L. Falasca, Evidences for lipid involvement in SARS-CoV-2 cytopathogenesis. *Cell Death Dis.* **12**, 263 (2021).
10. A. Signes, E. Fernandez-Vizarra, Assembly of mammalian oxidative phosphorylation complexes I-V and supercomplexes. *Essays Biochem.* **62**, 255–270 (2018).
11. S. Guerrero-Castillo, F. Baertling, D. Kownatzki, H. J. Wessels, S. Arnold, U. Brandt, L. Nijtmans, The assembly pathway of mitochondrial respiratory chain complex I. *Cell Metab.* **25**, 128–139 (2017).
12. A. B. Cuperfain, Z. L. Zhang, J. L. Kennedy, V. F. Goncalves, The complex interaction of mitochondrial genetics and mitochondrial pathways in psychiatric disease. *Mol. Neuropsychiatry* **4**, 52–69 (2018).
13. D. E. Gordon, J. Hiatt, M. Bouhaddou, V. V. Rezelj, S. Ulferts, H. Braberg, A. S. Jureka, K. Obernier, J. Z. Guo, J. Batra, R. M. Kaake, A. R. Weckstein, T. W. Owens, M. Gupta, S. Pourmal, E. W. Titus, M. Cakir, M. Soucheray, M. McGregor, Z. Cakir, G. Jang, M. J. O'Meara, T. A. Tummino, Z. Zhang, H. Foussard, A. Rojc, Y. Zhou, D. Kuchenov, R. Hüttenhain, J. Xu, M. Eckhardt, D. L. Swaney, J. M. Fabius, M. Ummadi, B. Tutuncuoglu, U. Rathore, M. Modak, P. Haas, K. M. Haas, Z. Z. C. Naing, E. H. Pulido, Y. Shi, I. Barrio-Hernandez, D. Memon, E. Petsalaki, A. Dunham, M. C. Marrero, D. Burke, C. Koh, T. Vallet, J. A. Silvas, C. M. Azumaya, C. Billesbølle, A. F. Brilot, M. G. Campbell, A. Diallo, M. S. Dickinson, D. Diwanji, N. Herrera, N. Hoppe, H. T. Kratochvil, Y. Liu, G. E. Merz, M. Moritz, H. C. Nguyen, C. Nowotny, C. Puchades, A. N. Rizo, U. Schulze-Gahmen, A. M. Smith, M. Sun, I. D. Young, J. Zhao, D. Asarnow, J. Biel, A. Bowen, J. R. Braxton, J. Chen, C. M. Chio, U. S. Chio, I. Deshpande, L. Doan, B. Faust, S. Flores, M. Jin, K. Kim, V. L. Lam, F. Li, J. Li, Y.-L. Li, Y. Li, X. Liu, M. Lo, K. E. Lopez, A. A. Melo, F. R. Moss III, P. Nguyen, J. Paulino, K. I. Pawar, J. K. Peters, T. H. Pospiech Jr., M. Safari, S. Sangwan, K. Schaefer, P. V. Thomas, A. C. Thwin, R. Trenker, E. Tse, T. K. M. Tsui, F. Wang, N. Whitis, Z. Yu, K. Zhang, Y. Zhang, F. Zhou, D. Saltzberg; QCRG Structural Biology Consortium, A. J. Hodder, A. S. Shun-Shion, D. M. Williams, K. M. White, R. Rosales, T. Kehrer, L. Miorin, E. Moreno, A. H. Patel, S. Rihn, M. M. Khalid, A. Vallejo-Gracia, P. Fozouni, C. R. Simoneau, T. L. Roth, D. Wu, M. A. Karim, M. Ghoussaini, I. Dunham, F. Berardi, S. Weigang, M. Chazal, J. Park, J. Logue, M. McGrath, S. Weston, R. Haupt, C. J. Hastie, M. Elliott, F. Brown, K. A. Burness, E. Reid, M. Dorward, C. Johnson, S. G. Wilkinson, A. Geyer, D. M. Giesel, C. Baillie, S. Raggett, H. Leech, R. Toth, N. Goodman, K. C. Keough, A. L. Lind; Zoonomia Consortium, R. J. Klesh, K. R. Hemphill, J. Carlson-Stevermer, J. Oki, K. Holden, T. Maures, K. S. Pollard, A. Sali, D. A. Agard, Y. Cheng, J. S. Fraser, A. Frost, N. Jura, T. Kortemme, A. Manglik, D. R. Southworth, R. M. Stroud, D. R. Alessi, P. Davies, M. B. Frieman, T. Ideker, C. Abate, N. Jouvenet, G. Kochs, B. Shoichet, M. Ott, M. Palmarini, K. M. Shokat, A. García-Sastre, J. A. Rassen, R. Grosse, O. S. Rosenberg, K. A. Verba, C. F. Basler, M. Vignuzzi, A. A. Peden, P. Beltrao, N. J. Krogan, Comparative host-coronavirus protein interaction networks reveal pan-viral disease mechanisms. *Science* **370**, eabe9403 (2020).
14. D. E. Gordon, G. M. Jang, M. Bouhaddou, J. Xu, K. Obernier, K. M. White, M. J. O'Meara, V. V. Rezelj, J. Z. Guo, D. L. Swaney, T. A. Tummino, R. Hüttenhain, R. M. Kaake, A. L. Richards, B. Tutuncuoglu, H. Foussard, J. Batra, K. Haas, M. Modak, M. Kim, P. Haas, B. J. Polacco, H. Braberg, J. M. Fabius, M. Eckhardt, M. Soucheray, M. J. Bennett, M. Cakir, M. J. McGregor, Q. Li, B. Meyer, F. Roesch, T. Vallet, A. Mac Kain, L. Miorin, E. Moreno, Z. Z. C. Naing, Y. Zhou, S. Peng, Y. Shi, Z. Zhang, W. Shen, I. T. Kirby, J. E. Melnyk, J. S. Chorba, K. Lou, S. A. Dai, I. Barrio-Hernandez, D. Memon, C. Hernandez-Armenta, J. Lyu, C. J. P. Mathy, T. Perica, K. B. Pilla, S. J. Ganesan, D. J. Saltzberg, R. Rakesh, X. Liu, S. B. Rosenthal, L. Calviello, S. Venkataramanan, J. Liboy-Lugo, Y. Lin, X. P. Huang, Y. F. Liu, S. A. Wankowicz, M. Bohn, M. Safari, F. S. Ugur, C. Koh, N. S. Savar, Q. D. Tran, D. Shengjuler, S. J. Fletcher, M. C. O'Neal, Y. Cai, J. C. J. Chang, D. J. Broadhurst, S. Klippsten, P. P. Sharp, N. A. Wenzell, D. Kuzuoglu-Ozturk, H. Y. Wang, R. Trenker, J. M. Young, D. A. Cavero, J. Hiatt, T. L. Roth, U. Rathore, A. Subramanian, J. Noack, M. Hubert, R. M. Stroud, A. D. Frankel, O. S. Rosenberg, K. A. Verba, D. A. Agard, M. Ott, M. Emerman, N. Jura, M. von Zastrow, E. Verdin, A. Ashworth, O. Schwartz, C. d'Enfert, S. Mukherjee, M. Jacobson, H. S. Malik, D. G. Fujimori, T. Ideker, C. S. Craik, S. N. Floor, J. S. Fraser, J. D. Gross, A. Sali, B. L. Roth, D. Ruggero, J. Taunton, T. Kortemme, P. Beltrao, M. Vignuzzi, A. García-Sastre, K. M. Shokat, B. K. Shoichet, N. J. Krogan, A SARS-CoV-2 protein interaction map reveals targets for drug repurposing. *Nature* **583**, 459–468 (2020).
15. A. Stukalov, V. Girault, V. Grass, O. Karayel, V. Bergant, C. Urban, D. A. Haas, Y. Huang, L. Oubraham, A. Wang, M. S. Hamad, A. Piras, F. M. Hansen, M. C. Tanzer, I. Paron, L. Zinzula, T. Engleitner, M. Reinecke, T. M. Lavacca, R. Ehmann, R. Wölfel, J. Jores, B. Kuster, U. Protzer, R. Rad, J. Ziebuhr, V. Thiel, P. Scaturro, M. Mann, A. Pichlmair, Multilevel proteomics reveals host perturbations by SARS-CoV-2 and SARS-CoV. *Nature* **594**, 246–252 (2021).
16. H. W. Jiang, Y. Li, H. N. Zhang, W. Wang, X. Yang, H. Qi, H. Li, D. Men, J. Zhou, S. C. Tao, SARS-CoV-2 proteome microarray for global profiling of COVID-19 specific IgG and IgM responses. *Nat. Commun.* **11**, 3581 (2020).
17. J. Wu, Y. Shi, X. Pan, S. Wu, R. Hou, Y. Zhang, T. Zhong, H. Tang, W. du, L. Wang, J. Wo, J. Mu, Y. Qiu, K. Yang, L. K. Zhang, B. C. Ye, N. Qi, SARS-CoV-2 ORF9b inhibits RIG-I-MAVS antiviral signaling by interrupting K63-linked ubiquitination of NEMO. *Cell Rep.* **34**, 108761 (2021).
18. S. Li, F. Ma, T. Yokota, G. Garcia Jr., A. Palermo, Y. Wang, C. Farrell, Y.-C. Wang, R. Wu, Z. Zhou, C. Pan, M. Morselli, M. A. Teitell, S. Ryazantsev, G. A. Fishbein, J. T. Hoeve, V. A. Arboleda, J. Bloom, B. Dillon, M. Pellegrini, A. J. Lusis, T. G. Graeber, V. Arumugaswami, A. Deb, Metabolic reprogramming and epigenetic changes of vital organs in SARS-CoV-2 induced systemic toxicity. *JCI Insight* **6**, e145027 (2021).
19. D. Bojkova, K. Klann, B. Koch, M. Widera, D. Krause, S. Ciesek, J. Cinatl, C. Münch, Proteomics of SARS-CoV-2-infected host cells reveals therapy targets. *Nature* **583**, 469–472 (2020).
20. B. Miller, A. Silverstein, M. Flores, K. Cao, H. Kumagai, H. H. Mehta, K. Yen, S. J. Kim, P. Cohen, Host mitochondrial transcriptome response to SARS-CoV-2 in multiple cell models and clinical samples. *Sci. Rep.* **11**, 3 (2021).
21. H. Medini, A. Zirman, D. Mishmar, Immune system cells from COVID-19 patients display compromised mitochondrial-nuclear expression co-regulation and rewiring toward glycolysis. *iScience* **24**, 103471 (2021).
22. A. C. Codo, G. G. Davanzo, L. B. Monteiro, G. F. de Souza, S. P. Muraro, J. V. Virgilio-da-Silva, J. S. Prodonoff, V. C. Carregari, C. A. O. de Biagi Junior, F. Crunfli, J. L. Jimenez Restrepo, P. H. Vendramini, G. Reis-de-Oliveira, K. Bispo dos Santos, D. A. Toledo-Teixeira, P. L. Parise, M. C. Martini, R. E. Marques, H. R. Carmo, A. Borin, L. D. Coimbra, V. O. Boldrini, N. S. Brunetti, A. S. Vieira, E. Mansour, R. G. Ulaf, A. F. Bernardes, T. A. Nunes, L. C. Ribeiro, A. C. Palma, M. V. Agrela, M. L. Moretti, A. C. Sposito, F. B. Pereira, L. A. Velloso, M. A. R. Vinolo, A. Damasio, J. L. Proença-Módena, R. F. Carvalho, M. A. Mori, D. Martins-de-Souza, H. I. Nakaya, A. S. Farias, P. M. Moraes-Vieira, Elevated glucose levels favor SARS-CoV-2 infection and monocyte response through a HIF-1α/glycolysis-dependent axis. *Cell Metab.* **32**, 437–446.e5 (2020).
23. S. Krishnan, H. Nordqvist, A. T. Ambikan, S. Gupta, M. Sperk, S. Svensson-Akusjärvi, F. Mikaeloff, R. Benfeitas, E. Saccon, S. M. Ponnan, J. E. Rodriguez, N. Nikouyan, A. Odeh, G. Ahlén, M. Asghar, M. Sällberg, J. Vesterbacka, P. Nowak, Á. Végvári, A. Sönnerborg, C. J. Treutiger, U. Neogi, Metabolic perturbation associated with COVID-19 disease severity and SARS-CoV-2 replication. *Mol. Cell. Proteomics* **20**, 100159 (2021).
24. X. Duan, X. Tang, M. S. Nair, T. Zhang, Y. Qiu, W. Zhang, P. Wang, Y. Huang, J. Xiang, H. Wang, R. E. Schwartz, D. D. Ho, T. Evans, S. Chen, An airway organoid-based screen identifies a role for the HIF1α-glycolysis axis in SARS-CoV-2 infection. *Cell Rep.* **37**, 109920 (2021).
25. M. Tian, W. Liu, X. Li, P. Zhao, M. A. Shereen, C. Zhu, S. Huang, S. Liu, X. Yu, M. Yue, P. Pan, W. Wang, Y. Li, X. Chen, K. Wu, Z. Luo, Q. Zhang, J. Wu, HIF-1α promotes SARS-CoV-2 infection and aggravates inflammatory responses to COVID-19. *Signal Transduct. Target. Ther.* **6**, 308 (2021).
26. R. Fukuda, H. Zhang, J. W. Kim, L. Shimoda, C. V. Dang, G. L. Semenza, HIF-1 regulates cytochrome oxidase subunits to optimize efficiency of respiration in hypoxic cells. *Cell* **129**, 111–122 (2007).
27. Y. Zhang, R. Guo, S. H. Kim, H. Shah, S. Zhang, J. H. Liang, Y. Fang, M. Gentili, C. N. O'. Leary, S. J. Elledge, D. T. Hung, V. K. Mootha, B. E. Gewurz, SARS-CoV-2 hijacks folate and one-carbon metabolism for viral replication. *Nat. Commun.* **12**, 1676 (2021).
28. K. M. Dodd, J. Yang, M. H. Shen, J. R. Sampson, A. R. Tee, mTORC1 drives HIF-1α and VEGF-A signalling via multiple mechanisms involving 4E-BP1, S6K1 and STAT3. *Oncogene* **34**, 2239–2250 (2015).
29. K. G. de la Cruz Lopez, M. E. Toledo Guzman, E. O. Sanchez, A. G. Carranca, mTORC1 as a regulator of mitochondrial functions and a therapeutic target in cancer. *Front. Oncol.* **9**, 1373 (2019).
30. P. J. Mullen, G. Garcia Jr., A. Purkayastha, N. Matulionis, E. W. Schmid, M. Momcilovic, C. Sen, J. Langerman, A. Ramaiah, D. B. Shackelford, R. Damoiseaux, S. W. French, K. Plath, B. N. Gomperts, V. Arumugaswami, H. R. Christofk, SARS-CoV-2 infection rewires host cell metabolism and is potentially susceptible to mTORC1 inhibition. *Nat. Commun.* **12**, 1876 (2021).
31. R. H. Houtkooper, L. Mouchiroud, D. Ryu, N. Moullan, E. Katsyuba, G. Knott, R. W. Williams, J. Auwerx, Mitonuclear protein imbalance as a conserved longevity mechanism. *Nature* **497**, 451–457 (2013).
32. E. Fessler, E. M. Eckl, S. Schmitt, I. A. Mancilla, M. F. Meyer-Bender, M. Hanf, J. Philippou-Massier, S. Krebs, H. Zischka, L. T. Jae, A pathway coordinated by DELE1 relays mitochondrial stress to the cytosol. *Nature* **579**, 433–437 (2020).

33. E. Fessler, L. Krumwiede, L. T. Jae, DELE1 tracks perturbed protein import and processing in human mitochondria. *Nat. Commun.* **13**, 1853 (2022).
34. X. Guo, G. Aviles, Y. Liu, R. Tian, B. A. Unger, Y. H. T. Lin, A. P. Wiita, K. Xu, M. A. Correia, M. Kampmann, Mitochondrial stress is relayed to the cytosol by an OMA1-DELE1-HRI pathway. *Nature* **579**, 427–432 (2020).
35. B. F. Teske, M. E. Fusakio, D. Zhou, J. Shan, J. N. McClintick, M. S. Kilberg, R. C. Wek, CHOP induces activating transcription factor 5 (ATF5) to trigger apoptosis in response to perturbations in protein homeostasis. *Mol. Biol. Cell* **24**, 2477–2490 (2013).
36. P. M. Quirós, M. A. Prado, N. Zamboni, D. D'Amico, R. W. Williams, D. Finley, S. P. Gygi, J. Auwerx, Multi-omics analysis identifies ATF4 as a key regulator of the mitochondrial stress response in mammals. *J. Cell Biol.* **216**, 2027–2045 (2017).
37. Y. L. Wong, L. LeBon, A. M. Basso, K. L. Kohlhaas, A. L. Nikkel, H. M. Robb, D. L. Donnelly-Roberts, J. Prakash, A. M. Swensen, N. D. Rubinstein, S. Krishnan, F. E. McAllister, N. V. Haste, J. J. O'Brien, M. Roy, A. Ireland, J. M. Frost, L. Shi, S. Riedmaier, K. Martin, M. J. Dart, C. Sidrauski, eIF2B activator prevents neurological defects caused by a chronic integrated stress response. *eLife* **8**, e42940 (2019).
38. Y. L. Wong, L. LeBon, R. Edalji, H. B. Lim, C. Sun, C. Sidrauski, The small molecule ISRIB rescues the stability and activity of vanishing white matter disease eIF2B mutant complexes. *eLife* **7**, e32733 (2018).
39. E. Balsa, M. S. Soustek, A. Thomas, S. Cogliati, C. García-Poyatos, E. Martín-García, M. Jedrychowski, S. P. Gygi, J. A. Enriquez, P. Puigserver, ER and nutrient stress promote assembly of respiratory chain supercomplexes through the PERK-eIF2α axis. *Mol. Cell* **74**, 877–890.e6 (2019).
40. S. Ajaz, M. J. McPhail, K. K. Singh, S. Mujib, F. M. Trovato, S. Napoli, K. Agarwal, Mitochondrial metabolic manipulation by SARS-CoV-2 in peripheral blood mononuclear cells of patients with COVID-19. *Am. J. Physiol. Cell Physiol.* **320**, C57–C65 (2021).
41. L. G. de Guadiana Romualdo, M. D. R. Mulero, M. H. Olivo, C. R. Rojas, V. R. Arenas, M. G. Morales, A. B. Abellán, P. Conesa-Zamora, J. García-García, A. C. Hernández, D. Morell-García, M. D. Albaladejo-Otón, L. Consuegra-Sánchez, Circulating levels of GDF-15 and calprotectin for prediction of in-hospital mortality in COVID-19 patients: A case series. *J. Infect.* **82**, e40–e42 (2021).
42. D. Butler, C. Mozsary, C. Meydan, J. Foox, J. Rosiene, A. Shaiber, D. Danko, E. Afshinnekoo, M. MacKay, F. J. Sedlazeck, N. A. Ivanov, M. Sierra, D. Pohle, M. Zietz, U. Gisladottir, V. Ramlall, E. T. Sholle, E. J. Schenck, C. D. Westover, C. Hassan, K. Ryon, B. Young, C. Bhattacharya, D. L. Ng, A. C. Granados, Y. A. Santos, V. Servellita, S. Federman, P. Ruggiero, A. Fungtammasan, C. S. Chin, N. M. Pearson, B. W. Langhorst, N. A. Tanner, Y. Kim, J. W. Reeves, T. D. Hether, S. E. Warren, M. Bailey, J. Gawrys, D. Meleshko, D. Xu, M. Couto-Rodriguez, D. Nagy-Szakal, J. Barrows, H. Wells, N. B. O'Hara, J. A. Rosenfeld, Y. Chen, P. A. D. Steel, A. J. Shemesh, J. Xiang, J. Thierry-Mieg, D. Thierry-Mieg, A. Iftner, D. Bezdan, E. Sanchez, T. R. Campion Jr., J. Sipley, L. Cong, A. Craney, P. Velu, A. M. Melnick, S. Shapira, I. Hajirasouliha, A. Borczuk, T. Iftner, M. Salvatore, M. Loda, L. F. Westblade, M. Cushing, S. Wu, S. Levy, C. Chiu, R. E. Schwartz, N. Tatonetti, H. Rennert, M. Imielinski, C. E. Mason, Shotgun transcriptome, spatial omics, and isothermal profiling of SARS-CoV-2 infection reveals unique host responses, viral diversification, and drug interactions. *Nat. Commun.* **12**, 1660 (2021).
43. D. J. Pagliarini, S. E. Calvo, B. Chang, S. A. Sheth, S. B. Vafai, S. E. Ong, G. A. Walford, C. Sugiana, A. Boneh, W. K. Chen, D. E. Hill, M. Vidal, J. G. Evans, D. R. Thorburn, S. A. Carr, V. K. Mootha, A mitochondrial protein compendium elucidates complex I disease biology. *Cell* **134**, 112–123 (2008).
44. S. Rath, R. Sharma, R. Gupta, T. Ast, C. Chan, T. J. Durham, R. P. Goodman, Z. Grabarek, M. E. Haas, W. H. W. Hung, P. R. Joshi, A. A. Jourdain, S. H. Kim, A. V. Kotrys, S. S. Lam, J. G. McCoy, J. D. Meisel, M. Miranda, A. Panda, A. Patgiri, R. Rogers, S. Sadre, H. Shah, O. S. Skinner, T. L. To, M. A. Walker, H. Wang, P. S. Ward, J. Wengrod, C. C. Yuan, S. E. Calvo, V. K. Mootha, MitoCarta3.0: An updated mitochondrial proteome now with sub-organelle localization and pathway annotations. *Nucleic Acids Res.* **49**, D1541–D1547 (2021).
45. A. Dhir, S. Dhir, L. S. Borowski, L. Jimenez, M. Teitell, A. Rötig, Y. J. Crow, G. I. Rice, D. Duffy, C. Tamby, T. Nojima, A. Munnich, M. Schiff, C. R. de Almeida, J. Rehwinkel, A. Dziembowski, R. J. Szczesny, N. J. Proudfoot, Mitochondrial double-stranded RNA triggers antiviral signalling in humans. *Nature* **560**, 238–242 (2018).
46. R. Wu, F. Chen, N. Wang, D. Tang, R. Kang, ACOD1 in immunometabolism and disease. *Cell. Mol. Immunol.* **17**, 822–833 (2020).
47. R. K. Gupta, J. Rosenheim, L. C. Bell, A. Chandran, J. A. Guerra-Assuncao, G. Pollara, M. Whelan, J. Artico, G. Joy, H. Kurdi, D. M. Altmann, R. J. Boyton, M. K. Maini, A. McKnight, J. Lambourne, T. Cutino-Moguel, C. Manisty, T. A. Treibel, J. C. Moon, B. M. Chain, M. Noursadeghi, H. Abbass, A. Abiodun, M. Alfarih, Z. Alldis, D. M. Altmann, O. E. Amin, M. Andiapen, J. Artico, J. B. Augusto, G. L. Baca, S. N. L. Bailey, A. N. Bhuva, A. Boulter, R. Bowles, R. J. Boyton, O. V. Bracken, B. O'Brien, T. Brooks, N. Bullock, D. K. Butler, G. Captur, N. Champion, C. Chan, A. Chandran, D. Collier, J. Couto de Sousa, X. Couto-Parada, T. Cutino-Moguel, R. H. Davies, B. Douglas, C. di Genova, K. Dieobi-Anene, M. O. Diniz, A. Ellis, K. Feehan, M. Finlay, M. Fontana, N. Forooghi, C. Gaier, J. M. Gibbons, D. Gilroy, M. Hamblin, G. Harker, J. Hewson, L. M. Hickling, A. D. Hingorani, L. Howes, A. Hughes, G. Hughes, R. Hughes, I. Itua, V. Jardim, W. Y. J. Lee, M. Jensen, J. Jones, M. Jones, G. Joy, V. Kapil, H. Kurdi, J. Lambourne, K. M. Lin, S. Louth, M. K. Maini, V. Mandadapu, C. Manisty, Á. McKnight, K. Menacho, C. Mfuko, O. Mitchelmore, C. Moon, J. C. Moon, D. Munoz Sandoval, S. M. Murray, M. Noursadeghi, A. Otter, C. Pade, S. Palma, R. Parker, K. Patel, B. Pawarova, S. E. Petersen, B. Piniera, F. P. Pieper, D. Pope, M. Prossora, L. Rannigan, A. Rapala, C. J. Reynolds, A. Richards, M. Robathan, J. Rosenheim, G. Sambile, N. M. Schmidt, A. Semper, A. Seraphim, M. Simion, A. Smit, M. Sugimoto, L. Swadling, S. Taylor, N. Temperton, S. Thomas, G. D. Thornton, T. A. Treibel, A. Tucker, J. Veerapen, M. Vijayakumar, S. Welch, T. Wodehouse, L. Wynne, D. Zahedi, Blood transcriptional biomarkers of acute viral infection for detection of pre-symptomatic SARS-CoV-2 infection: A nested, case-control diagnostic accuracy study. *Lancet Microbe* **2**, e508–e517 (2021).
48. N. Rother, C. Yanginlar, R. G. H. Lindeboom, S. Bekkering, M. M. T. van Leent, B. Buijsers, I. Jonkman, M. de Graaf, M. Baltissen, L. A. Lamers, N. P. Riksen, Z. A. Fayad, W. J. M. Mulder, L. B. Hilbrands, L. A. B. Joosten, M. G. Netea, M. Vermeulen, J. van der Vlag, R. Duivenvoorden, Hydroxychloroquine inhibits the trained innate immune response to interferons. *Cell Rep. Med.* **1**, 100146 (2020).
49. C. Q. E. Lee, B. Kerouanton, S. Chothani, S. Zhang, Y. Chen, C. K. Mantri, D. H. Hock, R. Lim, R. Nadkarni, V. T. Huynh, D. Lim, W. L. Chew, F. L. Zhong, D. A. Stroud, S. Schafer, V. Tergaonkar, A. L. St John, O. J. L. Rackham, L. Ho, Coding and non-coding roles of MOCCI (C15ORF48) coordinate to regulate host inflammation and immunity. *Nat. Commun.* **12**, 2130 (2021).
50. P. Fisel, E. Schaeffeler, M. Schwab, Clinical and functional relevance of the monocarboxylate transporter family in disease pathophysiology and drug therapy. *Clin. Transl. Sci.* **11**, 352–364 (2018).
51. N. A. Khan, J. Nikkanen, S. Yatsuga, C. Jackson, L. Wang, S. Pradhan, R. Kivelä, A. Pessia, V. Velagapudi, A. Suomalainen, mTORC1 regulates mitochondrial integrated stress response and mitochondrial myopathy progression. *Cell Metab.* **26**, 419–428.e5 (2017).
52. L. Liu, D. R. Wise, J. A. Diehl, M. C. Simon, Hypoxic reactive oxygen species regulate the integrated stress response and cell survival. *J. Biol. Chem.* **283**, 31153–31162 (2008).
53. J. T. McDonald, F. J. Enguita, D. Taylor, R. J. Griffin, W. Priebe, M. R. Emmett, M. M. Sajadi, A. D. Harris, J. Clement, J. M. Dybas, N. Aykin-Burns, J. W. Guarnieri, L. N. Singh, P. Grabham, S. B. Baylin, A. Yousey, A. N. Pearson, P. M. Corry, A. Saravia-Butler, T. R. Aunins, S. Sharma, P. Nagpal, C. Meydan, J. Foox, C. Mozsary, B. Cerqueira, V. Zaksas, U. Singh, E. S. Wurtele, S. V. Costes, G. G. Davanzo, D. Galeano, A. Paccanaro, S. L. Meinig, R. S. Hagan, N. M. Bowman, M. C. Wolfgang, S. Altinok, N. Sapoval, T. J. Treangen, P. M. Moraes-Vieira, C. Vanderburg, D. C. Wallace, J. C. Schisler, C. E. Mason, A. Chatterjee, R. Meller, A. Beheshti; UNC COVID-19 Pathobiology Consortium, Role of miR-2392 in driving SARS-CoV-2 infection. *Cell Rep.* **37**, 109839 (2021).
54. J. T. McDonald, F. J. Enguita, D. Taylor, R. J. Griffin, W. Priebe, M. R. Emmett, M. M. Sajadi, A. D. Harris, J. Clement, J. M. Dybas, N. Aykin-Burns, J. W. Guarnieri, L. N. Singh, P. Grabham, S. B. Baylin, A. Yousey, A. N. Pearson, P. M. Corry, A. Saravia-Butler, T. R. Aunins, S. Sharma, P. Nagpal, C. Meydan, J. Foox, C. Mozsary, B. Cerqueira, V. Zaksas, U. Singh, E. S. Wurtele, S. V. Costes, G. G. Davanzo, D. Galeano, A. Paccanaro, S. L. Meinig, R. S. Hagan, N. M. Bowman; UNC COVID- Pathobiology Consortium, M. C. Wolfgang, S. Altinok, N. Sapoval, T. J. Treangen, P. M. Moraes-Vieira, C. Vanderburg, D. C. Wallace, J. Schisler, C. E. Mason, A. Chatterjee, R. Meller, A. Beheshti, The great deceiver: miR-2392's hidden role in driving SARS-CoV-2 infection. bioRxiv 2021.2004.2023.441024 [preprint] (2021). https://doi.org/10.1101/2021.04.23.441024.
55. S. Fan, T. Tian, W. Chen, X. Lv, X. Lei, H. Zhang, S. Sun, L. Cai, G. Pan, L. He, Z. Ou, X. Lin, X. Wang, M. F. Perez, Z. Tu, S. Ferrone, B. A. Tannous, J. Li, Mitochondrial miRNA determines chemoresistance by reprogramming metabolism and regulating mitochondrial transcription. *Cancer Res.* **79**, 1069–1084 (2019).
56. Y. Zhang, M. S. Kim, E. Nguyen, D. M. Taylor, Modeling metabolic variation with single-cell expression data. bioRxiv 2020.01.28.923680 [preprint] (2020). https://doi.org/10.1101/2020.01.28.923680.
57. J. J. Frere, R. A. Serafini, K. D. Pryce, M. Zazhytska, K. Oishi, I. Golynker, M. Panis, J. Zimering, S. Horiuchi, D. A. Hoagland, R. Møller, A. Ruiz, A. Kodra, J. B. Overdevest, P. D. Canoll, A. C. Borczuk, V. Chandar, Y. Bram, R. Schwartz, S. Lomvardas, V. Zachariou, B. R. tenOever, SARS-CoV-2 infection in hamsters and humans results in lasting and unique systemic perturbations after recovery. *Sci. Transl. Med.* **14**, eabq3059 (2022).
58. S. R. Leist, K. H. Dinnon III, A. Schäfer, L. V. Tse, K. Okuda, Y. J. Hou, A. West, C. E. Edwards, W. Sanders, E. J. Fritch, K. L. Gully, T. Scobey, A. J. Brown, T. P. Sheahan, N. J. Moorman, R. C. Boucher, L. E. Gralinski, S. A. Montgomery, R. S. Baric, A mouse-adapted SARS-CoV-2 induces acute lung injury and mortality in standard laboratory mice. *Cell* **183**, 1070–1085.e12 (2020).
59. R. A. Grant, L. Morales-Nebreda, N. S. Markov, S. Swaminathan, M. Querrey, E. R. Guzman, D. A. Abbott, H. K. Donnelly, A. Donayre, I. A. Goldberg, Z. M. Klug, N. Borkowski, Z. Lu, H. Kihshen, Y. Politanska, L. Sichizya, M. Kang, A. Shilatifard, C. Qi, J. W. Lomasney, A. C. Argento, J. M. Kruser, E. S. Malsin, C. O. Pickens, S. B. Smith, J. M. Walter, A. E. Pawlowski,

D. Schneider, P. Nannapaneni, H. Abdala-Valencia, A. Bharat, C. J. Gottardi, G. R. S. Budinger, A. V. Misharin, B. D. Singer, R. G. Wunderink; The NU SCRIPT Study Investigators, R. A. Grant, L. Morales-Nebreda, N. S. Markov, S. Swaminathan, M. Querrey, E. R. Guzman, D. A. Abbott, H. K. Donnelly, A. Donayre, I. A. Goldberg, Z. M. Klug, N. Borkowski, Z. Lu, H. Kihshen, Y. Politanska, L. Sichizya, M. Kang, A. Shilatifard, C. Qi, J. W. Lomasney, A. C. Argento, J. M. Kruser, E. S. Malsin, C. O. Pickens, S. B. Smith, J. M. Walter, A. E. Pawlowski, D. Schneider, P. Nannapaneni, H. Abdala-Valencia, A. Bharat, C. J. Gottardi, G. R. S. Budinger, A. V. Misharin, B. D. Singer, R. G. Wunderink, A. A. Wagh, A. R. Hauser, A. R. Wolfe, A. Thakrar, A. V. Yeldandi, A. A. Wang, A. R. Levenson, A. M. Joudi, B. Tran, C. A. Gao, C. Kurihara, C. J. Schroedl, C. M. Horvath, D. Meza, D. D. Odell, D. W. Kamp, D. R. Winter, E. A. Ozer, E. D. Shanes, E. T. Bartom, E. J. Rendleman, E. M. Leibenguth, F. Wehbe, G. Y. Liu, G. T. Gadhvi, H. T. Navarro, J. I. Sznajder, J. E. Dematte, J. Ie, J. M. Arnold, J. C. du, J. Coleman, J. I. Bailey, J. S. Deters, J. A. Fiala, J. Starren, K. M. Ridge, K. Secunda, K. Aren, K. L. Gates, K. Todd, L. D. Gradone, L. N. Textor, L. F. Wolfe, L. L. Pesce, L. A. Nunes Amaral, M. L. Rosenbaum, M. Kandpal, M. Jain, M. A. Sala, M. Saine, M. Carns, M. J. Alexander, M. J. Cuttica, M. H. Prickett, N. H. Khan, N. S. Chandel, N. D. Soulakis, O. R. Rivas, P. C. Seed, P. A. Reyfman, P. D. Go, P. H. S. Sporn, P. R. Cooper, R. Tomic, R. Patel, R. Garza-Castillon, R. Kalhan, R. I. Morimoto, R. J. Mylvaganam, S. S. Kim, S. W. M. Gatesy, S. Thakkar, S. Ben Maamar, S. H. Han, S. R. Rosenberg, S. Nozick, S. J. Green, S. R. Russell, T. A. Poor, T. J. Zak, T. A. Lombardo, T. Stoeger, T. Shamaly, Z. Ren, Circuits between infected macrophages and T cells in SARS-CoV-2 pneumonia. *Nature* **590**, 635–641 (2021).

60. J. Kee, S. Thudium, D. M. Renner, K. Glastad, K. Palozola, Z. Zhang, Y. Li, Y. Lan, J. Cesare, A. Poleshko, A. A. Kiseleva, R. Truitt, F. L. Cardenas-Diaz, X. Zhang, X. Xie, D. N. Kotton, K. D. Alysandratos, J. A. Epstein, P. Y. Shi, W. Yang, E. Morrisey, B. A. Garcia, S. L. Berger, S. R. Weiss, E. Korb, SARS-CoV-2 disrupts host epigenetic regulation via histone mimicry. *Nature* **610**, 381–388 (2022).
61. J. W. Guarnieri, A. Angelin, D. G. Murdock, P. Schaefer, P. Portluri, T. Lie, J. Huang, D. C. Wallace, SARS-CoV-2 viroporins activate the NLRP3-inflammasome by the mitochondrial permeability transition pore. *Front. Immunol.* **14**, 1064293 (2023).
62. J. Li, O. T. Tran, T. B. Crowley, T. M. Moore, E. H. Zackai, B. S. Emanuel, D. M. McDonald-McGinn, R. E. Gur, D. C. Wallace, S. A. Anderson, Association of mitochondrial biogenesis with variable penetrance of schizophrenia. *JAMA Psychiatry* **78**, 911–921 (2021).
63. M. I. Love, W. Huber, S. Anders, Moderated estimation of fold change and dispersion for RNA-seq data with DESeq2. *Genome Biol.* **15**, 550 (2014).
64. J. Park, J. Foox, T. Hether, D. C. Danko, S. Warren, Y. Kim, J. Reeves, D. J. Butler, C. Mozsary, J. Rosiene, A. Shaiber, E. E. Afshin, M. MacKay, A. F. Rendeiro, Y. Bram, V. Chandar, H. Geiger, A. Craney, P. Velu, A. M. Melnick, I. Hajirasouliha, A. Beheshti, D. Taylor, A. Saravia-Butler, U. Singh, E. S. Wurtele, J. Schisler, S. Fennessey, A. Corvelo, M. C. Zody, S. Germer, S. Salvatore, S. Levy, S. Wu, N. P. Tatonetti, S. Shapira, M. Salvatore, L. F. Westblade, M. Cushing, H. Rennert, A. J. Kriegel, O. Elemento, M. Imielinski, C. M. Rice, A. C. Borczuk, C. Meydan, R. E. Schwartz, C. E. Mason, System-wide transcriptome damage and tissue identity loss in COVID-19 patients. *Cell Rep. Med.* **3**, 100522 (2022).
65. S. Tyanova, T. Temu, P. Sinitcyn, A. Carlson, M. Y. Hein, T. Geiger, M. Mann, J. Cox, The Perseus computational platform for comprehensive analysis of (prote)omics data. *Nat. Methods* **13**, 731–740 (2016).
66. K. D. Sullivan, M. D. Galbraith, K. T. Kinning, K. W. Bartsch, N. C. Levinsky, P. Araya, K. P. Smith, R. E. Granrath, J. R. Shaw, R. M. Baxter, K. R. Jordan, S. A. Russell, M. E. Dzieciatkowska, J. A. Reisz, F. Gamboni, F. I. Cendali, T. Ghosh, A. A. Monte, T. D. Bennett, M. G. Miller, E. W. Y. Hsieh, A. D'Alessandro, K. C. Hansen, J. M. Espinosa, The COVIDome explorer researcher portal. *Cell Rep.* **36**, 109527 (2021).
67. G. Korotkevich, V. Sukhov, N. Budin, B. Shpak, M. N. Artyomov, A. Sergushichev, Fast gene set enrichment analysis. bioRxiv 060012 (2021). https://doi.org/10.1101/060012
68. U. Singh, J. Li, A. Seetharam, E. S. Wurtele, pyrpipe: A Python package for RNA-Seq workflows. *NAR Genom. Bioinform.* **3**, lqab049 (2021).
69. U. Singh, M. Hur, K. Dorman, E. S. Wurtele, MetaOmGraph: A workbench for interactive exploratory data analysis of large expression datasets. *Nucleic Acids Res.* **48**, e23 (2020).
70. Z. Gu, R. Eils, M. Schlesner, Complex heatmaps reveal patterns and correlations in multidimensional genomic data. *Bioinformatics* **32**, 2847–2849 (2016).
71. Z. Gu, L. Gu, R. Eils, M. Schlesner, B. Brors, Circlize Implements and enhances circular visualization in R. *Bioinformatics* **30**, 2811–2812 (2014).
72. N. C. Duarte, S. A. Becker, N. Jamshidi, I. Thiele, M. L. Mo, T. D. Vo, R. Srivas, B. Ø. Palsson, Global reconstruction of the human metabolic network based on genomic and bibliomic data. *Proc. Natl. Acad. Sci. U.S.A.* **104**, 1777–1782 (2007).
73. A. Schultz, A. A. Qutub, Reconstruction of tissue-specific metabolic networks using CORDA. *PLoS Comput. Biol.* **12**, e1004808 (2016).
74. A. Subramanian, P. Tamayo, V. K. Mootha, S. Mukherjee, B. L. Ebert, M. A. Gillette, A. Paulovich, S. L. Pomeroy, T. R. Golub, E. S. Lander, J. P. Mesirov, Gene set enrichment analysis: A knowledge-based approach for interpreting genome-wide expression profiles. *Proc. Natl. Acad. Sci. U.S.A.* **102**, 15545–15550 (2005).

Acknowledgments

Funding: This work was supported by supplemental funds for COVID-19 research from Translational Research Institute of Space Health through NASA Cooperative Agreement NNX16AO69A (# T-0404 to A.B.) and funding from KBR Inc. (to A.B.). This work used resources, services, and support provided by the COVID-19 HPC Consortium (https://covid19-hpc-consortium.org/), specifically by the NASA High-End Computing (HEC) Program through the NASA Advanced Supercomputing (NAS) Division at Ames Research Center with funding awarded to A.B. This work was also supported by the Division of Intramural Research, NIAID, NIH (to S.M.B.) and, in part, by the Bill & Melinda Gates Foundation grant # INV-046722 (to D.C.W.). The opinions expressed in this article are those of the authors and do not reflect the views of the NIH, the Department of Health and Human Services, or the U.S. government. **Author contributions:** D.C.W. and A.B. conceived and directed the project. A.B. performed the computational analysis with input from D.C.W. and J.W.G. P.G. performed the miR-2392 mimic experiments in 3D HUVEC-MT cells. D.C.W. provided the conceptual bioenergetic framework for integrating the human and rodent data. A.S.-B., L.N.S., U.S., J.W.G., and J.H. assisted in statistical and computational analysis. J. Frere generated SARS-CoV-2–infected hamster data. C. Meydan, C. Mozsary, J. Foox, Y.B., R.E.S., and C.E.M. generated the human nasopharyngeal and autopsy tissue transcription data. M.T.H., N.J.M., V.K.B., E.A.M., S.A.T.-B., E.J.A., W.A.S., R.J.D., and J.C.S. generated the SARS-CoV-2 MA10–infected C57BL/6 and BALB/c mouse lung transcription data. S.D., V.S.-H., and M.S. developed QLattice analysis. D.C.W. and J.W.G. wrote the manuscript with input from A.B., E.S.W., and S.B.B. All authors read and reviewed the final version of the manuscript. **Competing interests:** R.E.S. is a paid consultant and on the scientific advisory boards of Miromatrix Inc. and Lime Therapeutics and is a consultant for Alnylam Inc. D.C.W. is a paid consultant and on the scientific advisory boards of Pano Therapeutics Inc. and Medical Excellent Capital. The other authors declare that they have no competing interests. **Data and materials availability:** All data associated with this study are present in the paper or the Supplementary Materials. Processed bulk RNA-seq data from the human nasopharyngeal samples and autopsy tissue samples are available at the dbGaP repository with accession number phs002258.v1.p1 and can be found at www.ncbi.nlm.nih.gov/projects/gap/cgi-bin/study.cgi?study_id=phs002258.v1.p1 and https://covidgenes.weill.cornell.edu/. The murine RNA-seq data are deposited in the Gene Expression Omnibus (GEO) repository with accession number GSE221510 and can be found at www.ncbi.nlm.nih.gov/geo/query/acc.cgi?acc=GSE221510. The murine RNA-seq data are also deposited in the NCBI BioProject database (www.ncbi.nlm.nih.gov/bioproject/) under the BioProject accession number PRJNA803057. The hamster RNA-seq data are deposited in the GEO repository with accession number GSE203001 and can be found at www.ncbi.nlm.nih.gov/geo/query/acc.cgi?acc=GSE203001. The RNA-seq data from the miR-2392 mimic 3D HUVEC-MT tissue model are available in the NASA Open Science Data Repository's Biological Data Management Environment (https://osdr.nasa.gov/bio/repo) with accession number OSD-577 and https://osdr.nasa.gov/bio/repo/data/studies/OSD-577. This research was funded in part by the Bill and Melinda Gates Foundation (grant # INV-046722), a cOAlition S organization. The authors will make the author-accepted manuscript (AAM) version available under a CC BY public copyright license.

Submitted 21 March 2022
Resubmitted 23 September 2022
Accepted 20 July 2023
Published 9 August 2023
10.1126/scitranslmed.abq1533

Science Translational Medicine

Core mitochondrial genes are down-regulated during SARS-CoV-2 infection of rodent and human hosts

Joseph W. Guarnieri, Joseph M. Dybas, Hossein Fazelinia, Man S. Kim, Justin Frere, Yuanchao Zhang, Yentli Soto Albrecht, Deborah G. Murdock, Alessia Angelin, Larry N. Singh, Scott L. Weiss, Sonja M. Best, Marie T. Lott, Shiping Zhang, Henry Cope, Victoria Zaksas, Amanda Saravia-Butler, Cem Meydan, Jonathan Foox, Christopher Mozsary, Yaron Bram, Yared Kidane, Waldemar Priebe, Mark R. Emmett, Robert Meller, Sam Demharter, Valdemar Stentoft-Hansen, Marco Salvatore, Diego Galeano, Francisco J. Enguita, Peter Grabham, Nidia S. Trovao, Urminder Singh, Jeffrey Haltom, Mark T. Heise, Nathaniel J. Moorman, Victoria K. Baxter, Emily A. Madden, Sharon A. Taft-Benz, Elizabeth J. Anderson, Wes A. Sanders, Rebekah J. Dickmander, Stephen B. Baylin, Eve Syrkin Wurtele, Pedro M. Moraes-Vieira, Deanne Taylor, Christopher E. Mason, Jonathan C. Schisler, Robert E. Schwartz, Afshin Beheshti, and Douglas C. Wallace

Sci. Transl. Med., **15** (708), eabq1533.
DOI: 10.1126/scitranslmed.abq1533

Science Translational Medicine (ISSN) is published by the American Association for the Advancement of Science. 1200 New York Avenue NW, Washington, DC 20005. The title *Science Translational Medicine* is a registered trademark of AAAS.